UNIVERSITY OF PADOVA

DEPARTMENT OF PHYSICS AND ASTRONOMY

Master degree in Astronomy

Orbital Study of Stellar systems with low mass companions

Supervisor: Prof. Sergio Ortolani
Co-supervisor: Doc. Riccardo Claudi
Co-supervisor: Doc. Silvano Desidera

Student: Francesco Maria Flammini Dotti
Matricola: 1106842

Contents

1 Disk and Exoplanets: Standard Model of Planet Formation **5**
- 1.1 Protoplanetary disk physics . . . 5
- 1.2 The Standard Model . . . 8
- 1.3 Planetary Migration . . . 12

2 Direct Imaging and instrumentation **17**
- 2.1 Direct Imaging . . . 17
  - 2.1.1 Adaptive Optics and High Contrast Imaging . . . 18
- 2.2 Project 1640 . . . 28
  - 2.2.1 Specifical Science of Project 1640 . . . 29
- 2.3 GPI . . . 30
  - 2.3.1 Instrument Description . . . 31
  - 2.3.2 Observation Modes . . . 32
- 2.4 SPHERE . . . 33
  - 2.4.1 Scientific goal and Target . . . 34
  - 2.4.2 Instruments Description . . . 35
  - 2.4.3 Observational Modes . . . 38

3 Computational approach to the problem **40**
- 3.1 HR8799, HD142527 and β Pictoris . . . 41
  - 3.1.1 HR8799 . . . 41
  - 3.1.2 β Pictoris . . . 43
  - 3.1.3 HD142527 . . . 44
- 3.2 From initial condition to the required epoch (Orbital elements of a visual binary) . . . 46
- 3.3 Montecarlo method . . . 48
- 3.4 Least Square fit . . . 49
- 3.5 χ^2_{red} verification . . . 50
- 3.6 Code description . . . 51
- 3.7 Application . . . 53

4 Scientific Results and theoretical confrontation **55**
- 4.1 HR8799 . . . 55
- 4.2 β Pictoris . . . 71
- 4.3 HD142527 . . . 73

5 Conclusion **83**

Introduction

The work of my Master Thesis is mainly focused on the study of objects with a transitional disk. The Standard Model for the planetary formation assumes that a star typically forms within a disk of debris and gas. The disks are heated by the star, and are observable in the infrared. These disks have a mean lifetime of the order of 5 million years, after which the disk is completely gone: the matter aggregates in planets or is taken into the star by gravitational attraction. The transitional disk is the phase after the planet formation and before the total disk dissipation. There are various hypothesis on the disk dissipation, but the most probable one is the gravitational attraction of the star.

The thesis discuss the structure of the disks around some young stars observed with SPHERE at VLT and GPI at Gemini South. After the description of the instruments and the observations, we present the application of a code for the orbit calculation.

The observed stellar systems are HR8799, a disk with 4 confirmed planets, Beta Pictoris, disk and a confirmed planet, and finally HD 142527, a binary system with an inner and outer disk separeted by a 100 *au* gap. The code is tested for HR8799 and Beta Pictoris, while was used as a specific study case for HD 142527.

The theoretical analysis includes the accretion disk physics, the gas proprieties, the dynamics, the thin and thick disk approssimation. Moreover the Planet Migration, one of the most important plug-ins of the Standard Model, is examined.

The observational data are producted with the High Contrast Imaging tecnique. This one is the direct heir to the Direct Imaging tecnique: they both use the Adaptive Optics, with the exception of the Coronagraph. This is fundamental for the images and it's followed by another important post-observation tecnique: the Speckle Suppression. Finally there is the description of SPHERE and GPI, which both use the High Contrast Imaging tecnique. Also it is described the "Project 1640", which aim is to study the architecture of some objects, like disks.

The last part is the original contribution of this thesis: the code and its application. It can be explained in two step:

1. Comparison between the literature data (that are taken in order to have an orbital parameter estimate). In order to do so, the Least Square Method is used and

therefore curves (orbits) of data confrontation are obtained. If the points pass into this orbits (or the points's error bars), the datas are good for the following Monte Carlo Method. There is, in the end, also a χ^2_{red} test.

2. It's possible to choose a range of random generated data in which the Monte Carlo Method operates: this value must be within the data literature estimate value, for obvious reasons. The purpose is double: the first aim is to verify that the confidence interval is right: there is also some use of the Monte Carlo method for the interval limits, in order to verify new possible data thanks to more precise astrometric data. The second step is to find parameters correlation. The Monte Carlo Method is then repeated again. As a filter for the false data, there is the χ^2_{red} test. The limit value of this parameter is set to 2.0.

The study case is the gap between the inner and outer disk in HD 142527. The code can find out if the star companion is the effective responsible for that. In the end we conclude that the most probable solution to this problem is the planet formation. Observation and further studies must be done in order to confirm that hypotesis.

The layout of the Master Thesis is:

Chapter 1: An insight on the theoretical point of view, where the Standard Model and his plug-ins and the general physics of an accretion disk are analyzed, including also the Planet Migration.

Chapter 2: The subsystem concept of each instrument and the scientific drivers are described: the Adaptive optics, the coronagraph and finally the speckle suppression are also described. The used instrumentation will be also described: GPI (Gemini Planet Finder) and SPHERE (Spectro-polarimetric High-contrast Exoplanet Researcher). Finally Project1640 is presented.

Chapter 3: Explanation of the code, giving focus on the main points that describe the code for the orbit's calculation. Moreover, there will be a brief description of the chosen stellar systems.

Chapter 4: In this chapter there is the analysis and confrontation of the data found by the code.

Chapter 5: Conclusions on the results of the previous chapter

Chapter 1

Disk and Exoplanets: Standard Model of Planet Formation

1.1 Protoplanetary disk physics

In order to completely understand the Standard Model, it is necessary to explain some physical proprieties of the protoplanetary and transitional disk. The former one is filled with gas and debris, while the latter is filled only with the debris remnants after the protoplanets formation.

The proto-planetary disks are an inevitable consequence of angular momentum conservation during the formation of a star through gravitational collapse.

As in [fig:1.1], the star forms within a cyclic process. Diffuse molecolar clouds merge creating a bigger one. The gravitational collapse of the inner parts of this cloud creates dense clumps. If the mass in one of them is enough, it starts to burn light elements, rapidly accreating gas and debris from the molecolar cloud. In this way the proto-star and the disk are created [2].

Because disks exhibit a range of temperatures, they radiate strongly at a range of wavelengths from microns to millimeters. They can therefore be observed with infrared and radio telescopes and the mapping of wavelength to radius allows detailed models of their structure. The Standard Model, which will be explained later, depict that the ratio between gas and dust is $\frac{1}{1000}$[3]. Also, the matter is considered as a fluid and $M_{star} \gg M_{disk}$.

The disk can be thought as a set of consecutive various rings with different angular velocity, which it's assumed Keplerian for the disk:

$$\Omega = \sqrt{\frac{GM_{star}}{R^3}} \tag{1.1}$$

The inner surface between the different rings will have a friction momenta which slows down the rings: if a test particle is taken, this one has a loss in the angular momenta $L = \sqrt{GM_{disk}R}$ and a subsequent reduction of R. In other words the particle falls down on the inner parts of the disk. In order to do so the different rings rotation

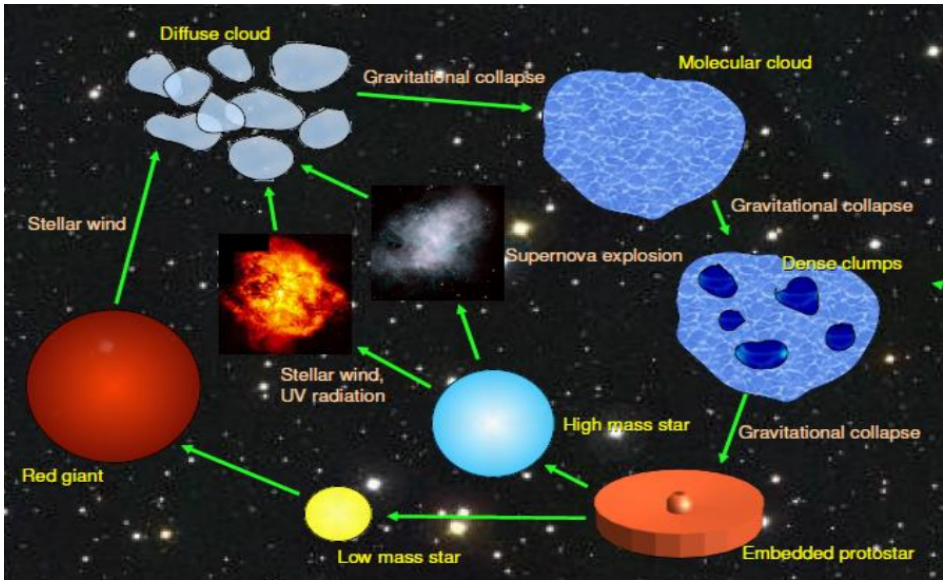

Figure 1.1: Star formation cycle

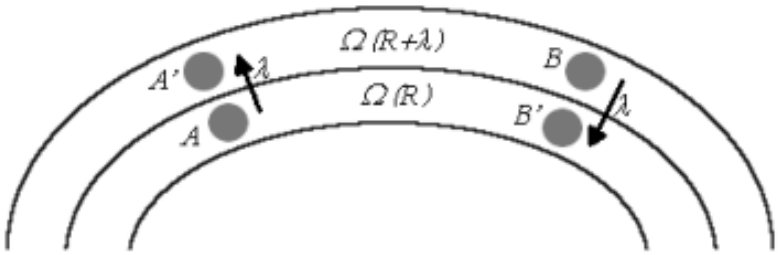

Figure 1.2: Graphical representation of bubbles motion in a turbulent state. Image by Taverna notes

must be differential.

The matter is in a turbulent state, in which the viscosity effects prevail over the general motion of the disk: the Reynold number ($R_e = \frac{\Omega \lambda R}{\nu}$, where ν is the kinematic viscosity and λ the linear minimum length of interation between the disk fluid elements) is the ratio between the inertial and viscous motions. In this system R_e is on the order of 10^{10}, so the system is indeed turbulent. [1]

The friction momenta is calculated by considering small elements, which are bigger than the molecular fluid elements, called bubbles (or simply fluid element) that are responsible for the friction mechanism. These bubbles retains the same thermodinamic and kinematic proprieties from the ring in which they are. For the angular momentum conservation in a close system, the bubbles moves both inward and outward [fig: 1.2].

The A bubble has a specific angular momentum of $L_A = \Omega(R)\ R(R + \lambda)$ while the

B one $L_B = \Omega(R+\lambda)\ R(R+\lambda)$. The material flux that accreate on the disk is $\Phi = v\rho$, where v is the bubble velocity and ρ the disk density. If it's consider the surface region in which the gas flows into the disk as a cilinder with height H and radius R, the dissipative momenta is [1]:

$$\tau = [\Omega(R)\ R(R+\lambda) - \Omega(R+\lambda)\ R(R+\lambda)]2\pi RH\rho v \tag{1.2}$$

The main physical properties of the disk follow a power-based law. They are the superficial density Σ and the disk temperature T, both dependent on the radius R. Considering the thin disk approssimation

$$\Sigma = \Sigma_0 \Big(\frac{R}{R_0}\Big)^{\alpha} \tag{1.3}$$

$$T = T_0 \Big(\frac{R}{R_0}\Big)^{\beta} \tag{1.4}$$

where the 0 subscript indicates the star parameter [3]. The thin disk approssimation describe a disk which vertical lenght component (H) is far smaller than its radius (R). The superificial density is commonly picked with the exponent equal to $\alpha = 10^{-2} - 10^{-3}$ [3] for the Standard Model, which is calculated in a molecolar cloud collapse model.

In general, for the calculation of the kinematic viscosity parameter, is used the $\alpha-$prescription:

$$\nu = \alpha H c_s \tag{1.5}$$

where α describes all the fluid uncertainties, H is the vertical length of the disk and c_s is the sound velocity in the fluid. In the most general view of the kinematic viscosity argument, the α parameter for the disk object is strictly model dependent, so it has various possible values.

The main idea is that in a normal ideal gas, viscosity is due to molecules that after moving some mean free path λ collide with another molecule exchanging momentum between them. This allows to transport momentum over small, but non-negligible, distances. In a turbulent flow (like the disk) the turbulent eddies also have a certain "mean free path" L, that is the distance they travel before they dissipate. In this enviroment $L \gg \lambda$.

Taking into account Eq 1.3, it's possible to calculate the optical depth and the mass:

$$\tau_\nu = k_\nu \Sigma = 0.1 \Big(\frac{\nu}{10^{12}\ Hz}\Big)^{\gamma} \Sigma_0 \Big(\frac{R}{R_0}\Big)^{\alpha} \tag{1.6}$$

$$M_{disk} = \frac{d^2 F_\nu}{B_\nu k_\nu} \tag{1.7}$$

$k_\nu = 0.1 \Big(\frac{\nu}{10^{12}\ Hz}\Big)^{\gamma}\ cm^2\ g^{-1}$ commonly describe the dust opacity at millimeter wavelengths, in which the exponent γ is related to the size, distribution and composition

of the dust grains. Eq 1.7 takes into account that the disk emits as a black body ($B_\nu = 2\frac{\nu^2 kT}{c^2}$) in the Raylegh-Jeans region of the spectrum. Finally d is the distance from the source and F_ν the monochromatic flux.[3]

The vertical component hydrostatic equilibrium's formula can be used to calculate the vertical evolution of the disk from the inside. The gravitational component of the formula is $g_z = -\frac{GM}{R^2}\sin(\theta)$. So:

$$\frac{1}{\rho}\frac{\partial P}{\partial z} = -\frac{GM}{R^2}\frac{z}{R} \tag{1.8}$$

where $\sin(\theta) = \frac{z}{R}$. The pression is:

$$P = \frac{kT\rho}{\mu m} \tag{1.9}$$

that is the ideal gas pressure, in which μ is the mean molecolar weight, d the Boltzmann costant and m is the proton mass. The temperature is considered to varies little in the z direction, so $T(z) = T_c$, where T_c is the temperature of the star [1].

Solving the differential equation, the final result is:

$$\rho = \rho_c e^{\frac{-Az^2}{2}} \tag{1.10}$$

where $A = \frac{\mu G M_{disk} m}{2kT_c R^3}$: M_{disk} is the disk mass, T_c the temperature of the star.[1]

The superficial density expressed in Eq. 1.3 it's good only in thin disk approssimation. The disk vertically evolves as an exponential (Eq 1.10)[3]:

$$\Sigma = (2-\eta)\frac{M_{disk}}{2\pi R^2}\Big(\frac{R}{R_c}\Big)^{\eta}\exp\Big(-\frac{R}{R_c}\Big)^{2-\eta} \tag{1.11}$$

where M_{disk} is the disk mass, R_c is the characteristic radius of the disk, and η specifies the radial dependence of the disk viscosity $\xi \propto R^{-\eta}$ and it is dependent on the viscous fluid proprieties.

1.2 The Standard Model

One of the best way to describe the planet formation was indentified in the Standard Model. However the subsequent discoveries arise the need to have some additions to the theory: they were named plug-ins as showed in [fig: 1.3].

The evolution process can be divided in two simple phases: the accretion phase and the evaporation phase. However the overall Standard Model is more complicated.

- Internal friction, or viscosity, within the disk drives continued accretion onto the star. To preserve angular momentum, the disk gradually spreads out with time. Its structure may also be strongly affected by photoevaporation, both from the central star and external stars, and the agglomeration of dust grains well beyond the typical sizes, found in the interstellar medium including, ultimately, planetesimals large enough to gravitationally perturb the disk. The various evolutionary

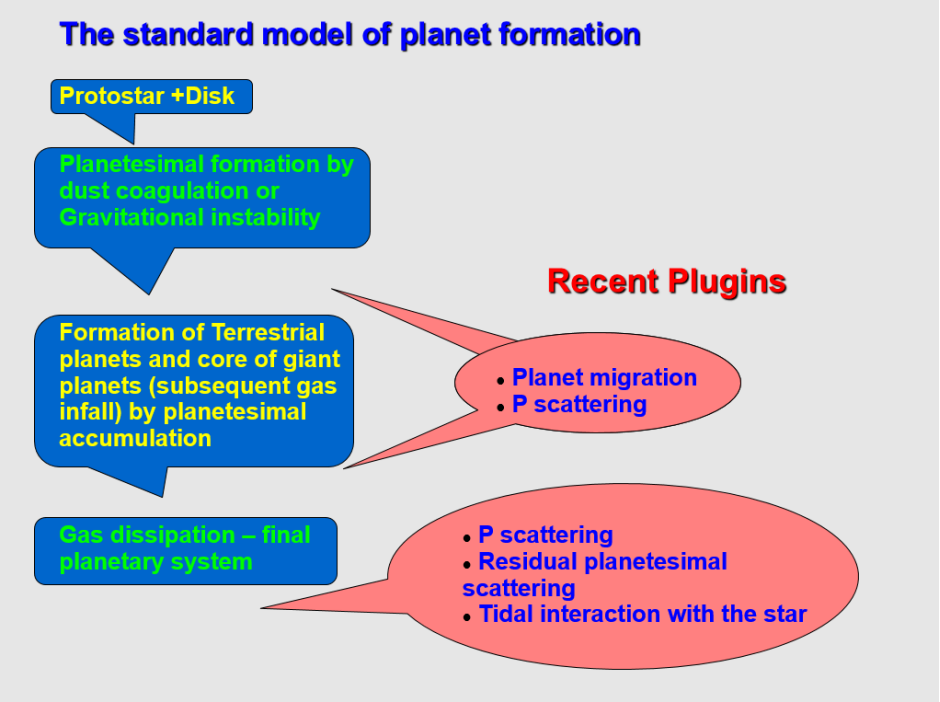

Figure 1.3: The Standard Model and its plug-ins. The P-Scattering indicates the planetesimal-planetesimal scattering. Image by Marzari Lectures

pathways lead to inner holes and gaps that reveal themselves through a relative decrement in flux over a narrow range of wavelengths and which may also be imaged directly at sufficiently high angular resolution. The situation at this stage can be seen in [fig 1.4].

- After accreting all the gas from the molecular nebula (in $t \sim 0.5\ Myr$), the situation is more "quiet", without gas outflows. A protoplanetary disk is matter (formed by gas and debris for the most part) orbiting around the star. This is possible thanks to the accretion power, that helds the rotation momenta of the particle against the gravitational attraction of the star. In this way it's plausible to assume that the final result of the accretion phenomena is a disk in the single star system.

- The third step is the coagulation of the particles into proto-planets (planetesimal aggregation, via p-scattering) or the same via gravitational instability. The main problem of the Standard Model stands in particular on this third point: planetesimal are proven to be really difficult to merge together. For example: in the Solar System, it has been proven that particles with a linear length lesser than 10 cm cannot merge cause of their elevated velocity (it has been see in every possible low or high density model of the Solar System done so far [4]). This stage of the proto-planets formation theory can be described with the following three elements:

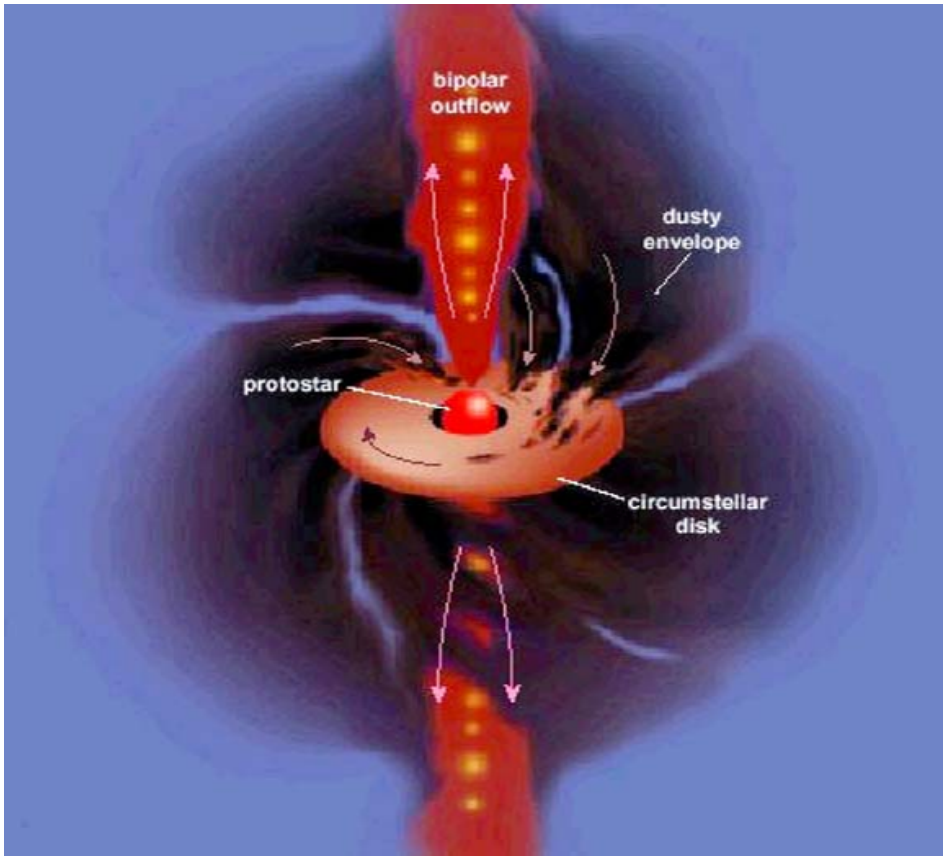

Figure 1.4: Initial evolution of the protostellar disk. There is a inflow gas thanks to the dusty envelope that surrounds the star. Meanwhile there is a bipolar outflow derived by the intense magnetic field. Image by Marzari lectures

1. Stream Instability: the fluid gas is not in hydro-dynamic equlibrium and the instabilities create smaller (or bigger) aggregation of particles. Johansen and Youdin (2007) showed that solid particles can, via magneto-rotational turbulence, aggregate those particles into planetesimal or bigger elements. More than one type of phenomena is created via magneto-rotational turbulence: giant vorticies, gas spirals and inner smaller disks. The aggregation result from cm-size pebbles to bodies 100-200 km in size.
2. Turbulences: These are zones in which a local turbulence creates an aggregation of particles: if that one is massive enough, it creates a giant planet core otherwise it creates a terrestrial-like core. Planet formation models typically treat turbulence as a diffusive process that opposes the gravitational sedimentation of solids to a high density midplane layer in circumstellar disks
3. Non destructive scattering between planetesimal: there is an anaelastic scattering between particles that creates an accumulation resulting in a core

The theory explained before is the Accretion Model. In this model a rocky core forms through the coagulation of planetesimals until it is sufficiently massive to accreate a gaseous envelope. Initially, this envelope is in hydrostatic equilibrium, with most of the luminosity provided by the accreting planetesimals. Once the core reaches a critical mass, however, hydrostatic equilibrium is no longer possible, and a phase of rapid gas accretion occurs.

There are, however, a number of issues with this model for the giant planets. The dust grains from which the planetesimals form may undergo a phase of rapid inward migration as soon as they reach a certain size. A rocky core itself, once it reaches about an Earth mass, should also migrate inwards rapidly, and upper limits for Jupiter's core are smaller than most theoretical estimates. Detailed models also predict growth timescales that may easily exceed the lifetime of the gaseous disk from which the planet formed [5].

A second theory was derived from the study of self-gravitating disks. Richard Nelson and John Papaloizou (2007) have also suggested that the core may undergo a random walk, rather than migrating in a single direction. What it's found, when including this random walk in the standard core accretion model, is that the core growth accelerates and reaches a critical mass far more quickly than if the core is assumed to remain stationary. What is more, when the planetesimal density is reduced slightly, the critical core mass is consistent with Jupiter's measured core mass.

- The fourth phase is when the planetesimal merges together building a protoplanet. A protoplanet is the previous evolutionary state of a planet: its orbit is still full of debris.
- The fifth step is the matter dissipation. There are multiple theories, as planetesimal violent scattering and tidal interactions. However the star type and the disk composition affect greatly this outcome.

- Before analyizing the sixth phase of protoplanet formation, it's necessary to introduce the Snow Line: it is the particular distance in the stellar nebula from the central protostar where it is cold enough for volatile compounds like water, ammonia, methane, carbon dioxide, carbon monoxide (elements taken as an example from the Solar System) to condense into solid ice grains. This condensation temperature depends on the volatile substance and the partial pressure of vapor in the protostar nebula. The actual temperature and distance for the snow line of water ice depend on the physical model used to calculate it and on the theoretical stellar nebula model. The type of elements are strictly dependent on the molecolar cloud composition.

- There is a final point to analyze: the planet effective formation and characterization. Following different planet's inside theories, the final solution suggest that:

    1. Rocky planets form themselves close to the star, before the snow line.
    2. Giant planets generate far away from the star, after the snow line. They are believed to be formed by a tiny, in respect of the entire planet, core, a intermediate liquid envelope (H and He) and an outer envelope formed by gas.

There are not particular conditions on the star, because planets have been observed orbiting around stars of every spectral type.

1.3 Planetary Migration

There is an important addition to the Standard Model of Planetary Formation: the Planetary Migration. It should explain why there are giant planets near the star instead of being after the Snow line.

There are also planet, called free-floating planets, that are not gravitationally bound to the star. It is highly possible that this phenomena regards the outward motion of the planetary migraton, but in this work it will be only analyzed the inner one.

This theory has two different initial situation: one where the planet is massive enough to create a gap in the disk (type II migration) or is small and do not create it (type I migration). As a consequence the first are gaseous giant planets, the second rocky planets and giant's cores. There is also a third type, actually a lot different in respect of the first two.

Type II migration

The gap formation inside a protoplanetary disk is explained by the Standard Model: the planet, either via gravitational instability or via planetesimals scattering takes the gas near his formation point. Clearly the more massive the planet, the bigger the gap

in the disk. When the gap is big enough, the outward flux of angular momentum due to viscous transport in the outer disk section is supplied by the planet. Similarly, the outward flux from the inner section is taken up by the planet. When these contributions do not balance, the planetary orbit changes its angular momentum and thus migrates. Normally, simulations indicate that the outer disk has the dominant effect, causing inward migration. In this case, the protoplanet was allowed to accrete as it migrated inwards on the viscous timescale of $\sim 10^5\ yr$. Inward migration on the viscous timescale $\frac{R^2}{v}$ is characteristic of type II migration driven by the evolution of the disk when the protoplanet mass does not exceed the local disk mass. In that case, using the standard α-prescription, the migration timescale is given by [5].

$$t_{mII} = \frac{1}{3\alpha}\left(\frac{R}{H}\right)^2 \Omega^{-1}\ yr \tag{1.12}$$

where R is the disk radius, H the vertical length of the disk, and finally Ω the Keplerian angular velocity of the disk fluid. If mean values for $\frac{H}{r} = 0.1$ and α are in the range $10^{-3} - 10^{-2}$, then $t_{mII} \sim 10^3\ yr$ and $10^4\ yr$ at $R = 1\ au$ and $5\ au$, respectively. These timescales are much shorter than the disk lifetime or the estimated planetary formation timescales. The time does not depend by the protoplanet's mass and the surface mass density of the disk, but it is implicitly assumed that the mass of gas within the orbital radius of the planet is at least comparable to the mass of the planet itself because the migration process starts if the disk is significantly less massive, and the inertia of the planet slows down the migration.

In order to stop the inward migration there are some possible situations:

- These planets would stop before falling onto the star if they entered its magnetospheric cavity.
- Tidal interaction with a rapidly rotating star would also halt planet orbital decay at a few stellar radii.
- A planet overflowing its Roche lobe and losing part of its mass to the central star would also halt at small orbital radii. This because during the transfer of mass the planet moves outwards to conserve the angular momentum of the system. The planet stops at the location where its physical radius is equal to its Roche radius.
- The resonance mechanism. In this case the planet real anomaly and the star rotation can have a proportional molteplicity: the drag forces are, in that way, halted and so the orbit of the planet became stable.

It has been suggested that migration of a giant planet could be stopped at any radius if migration and disk dissipation were concurrent. If the disk dissipates while migration is taking place, then the drift timescale may increase in such a way that the planet stalls at some finite radius.

Type I migration

This case concerns protoplanets that are not massive enough to form a gap in the disk: the rocky planets and the core of giant ones. The calculation of the linear response of the disk to an embedded orbiting protoplanet is used to calculate the angular momentum exchange rate with the protoplanet. The perturbation exerted by the protoplanet on the disk propagates as density waves outside the Lindblad resonances and is evanescent inside these resonances, in the co-rotation region. A Lindblad resonance is an orbital resonance in which an object's epicyclic frequency (the rate at which one periapse follows another) is a simple multiple of some forcing frequency. Resonances of this kind tend to increase the object's orbital eccentricity and to cause its longitude of periapse to line up in phase with the forcing. An example of the Lindblad resonances is found in Saturn's rings (where ring particles are subject to forcing by Saturn's moons).

The protoplanet exerts a torque on the density waves, which, together with the torque exerted at corotation, is responsible for the exchange of angular momentum between the disk rotation and the planet's orbital motion. Away from the Lindblad resonances, the waves have a small wavelength, so that the contribution to the net torque is small.

The conditions for the gap formation have been explored in a computational way. One model considers the MHD turbulence with zero net magnetic flux. The transition from being embedded to opening a gap occurs when this flux is around the unity and it corresponds to the gap formation condition mentioned in Paploizu et al 2005, which explains that the Hill sphere's radius should exceed the disk thickness.

Considering the situation explained above, the migration timescale is:

$$t_{mI} = 2(2.7 + 1.1\gamma)^{-1} \frac{M_\odot}{M_p} \frac{M_\odot}{\Sigma R^2} \left(\frac{H}{R}\right)^2 \Omega^{-1} \tag{1.13}$$

where $M_\odot$ is the mass of the Sun, and γ is a costant that takes into account all the proprieties of the viscous fluid, but it's for a thick disk situation. This timescale decreases linearly with mass, resulting in a survival problem for the core of giant planets. There is also a non-linearity given by γ In this context, even the smallest cores considered of 5 $M_\oplus$ have an infall timescale of only 2 10^5 yr. The γ factor is dependent by the chemical and physical proprieties of the disk.

Considering the turbulence created by the field, the subsequent migration can be described as stochastic. In this case the migration direction of small mass cores becomes unknown over the timescales. The performed simulations have an outcome that confirms that point: the direction is dependent on long term global fluctuations in the MHD turbulences which in turn depend on the global disk enviroment [5]. Also an investigation by Nelson (2005) suggest that turbulent fluctuations occour on all time scales up to the global diffusion or viscous time. Furthermore, the disk gas perturbed by the planet has a motion very different from laminar because of the large density fluctuations, encountering the planet. It provides stochastic torques when unperturbed by the planet.

Moreover, under some circumstances, significant fluctuations that can affect migration may occur in the non-magnetic case for planets with about the Saturn mass

through the production of instabilities in inviscid gap edges.

Type III migration

All the conclusion that will be described here are from the Papoloizu et al (2007). The third planet migration theory states that planets interact with large-scale vortices within the disk. But other interpretations than that exist, which are based on the circulation of co-orbital material during the migration of the planet [7]. This regime of migration may only applies to planets that can open partial gaps (via tidal interactions) in the disk.

Originally, the co-orbital material was thought to come from gas streaming across the orbit of the planet, in the opposite direction as the planet's radial motion.

More recently, it was discovered that the torques drive this mode of migration. It was associated to the gas trapped in the libration regions and moving radially with the planet. In particular, the torques arise from a density asymmetry between the gas on the leading and the trailing side of the planet, which is developed in response to the planet's radial motion.

In this assestment, the torque it's considered the principal responsible of the migration coorbital torque, or, better, a torque exerted on the protoplanet by disk material flowing through the orbit. One starts by considering a migrating protoplanet. When gap formation is only partial, material will flow through the orbit. As it does so, a torque will be exerted on the protoplanet. This may either act to assist the migration (positive feedback) or retard it (negative feedback). A study on Saturn revealed that only slow third type migration differs marginally from type II migration.

This was claimed to be the result from important torques acting within the Roche lobe [5].

The study of the migration of these partially gaps reveal that they form planets of modest mass, with a disk mass comparable to their own in the coorbital region [5].

Summarizing all the migration types:

- **Type I**: planets can drive spiral density waves in the surrounding gas or planetesimal disk, via their perturbing gravitational potential. In this case, the disk response to this perturbation is linear. An imbalance occurs in the strength of the interaction with the spirals inside and outside the planet's orbit. In most cases, the outer wave exerts a somewhat greater torque on the planet than does the interior wave. This causes the planet to lose orbital angular momentum and the planet then migrates inwards on timescales that are initially short relative to the million-year lifetime of the disk. Torques are also exerted by gas co-rotating with the planet, which shares the same orbit as (or a proximate orbit to) the planet.

- **Type II**: as giant cores begin to accreate matter, the type I migration for them stops. However, this creates a larger gap and the planet is pushed inward. The

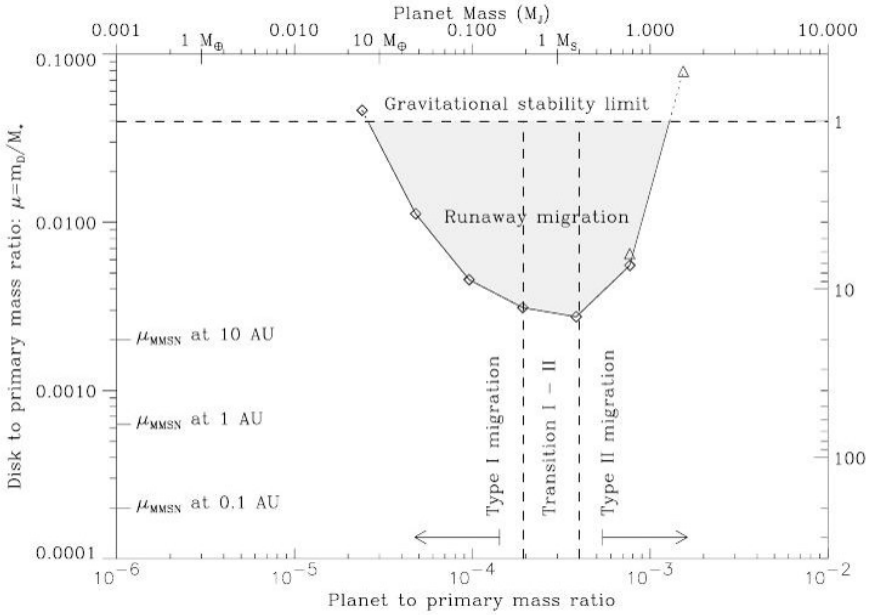

Figure 1.5: Planetary Migration summary: the MMSN (Minimum Mass Solar Nebula) is the model in use for the protoplanetary disk, but specifical of the Solar System formation data. Image by Marzari lectures

transition between Type I and Type II migration is generally smooth, but deviations from a smooth transition have also been found [6]

- **Type III**: planets interact with large-scale vortices within the disk or there is a circulation of co-orbital material during the migration of the planet (as recent study suggests). This regime of migration may only apply to planets that can open partial gaps (via tidal interactions) in the gas surface density of the disk.

A graphical summmary of the planet migration, at least for the first two types, is in [fig: 1.5]. The results are limited to the solar system and similar ones.

The runaway migration is the other hand of the first two migration explored here, and it's where the planet escape the stellar system. The gravitational stability limit is instead a limit for the stability on the planet orbit. For disk masses greater than that value, the planet would have an unstable orbit.

Chapter 2

Direct Imaging and instrumentation

2.1 Direct Imaging

The direct imaging is one of the method to search for exoplanets. Direct imaging means the direct detection of the radiation coming from the planet and/or disk, picked out from under the glare of the parent star [fig:2.1]. In this way it is possible to analyze the light reflected by the planet (visible) and also the intrinsic distribution of radiation emitted by the planet itself (infrared). In particular, direct imaging offers the possibility of determining the colors and spectra of a large number of planets, independently by their orbital inclination.

The first important thing to take into account in the direct imaging is the high angular resolution. For example, in the Jupiter-Sun case, if an observer is at 10 pc from them, the separation between the planet and the star would be 0.5 *arcsec* and the planet is swamped by the star glare. So to observe this system, it's necessary to use a telescope near the diffraction limit ($\theta = \frac{\lambda}{D}$).

The second quantity is the contrast or the ratio between the star and planet brightness. For example the contrast of the Earth with respect the Sun is of 10^{-10} in the visible and 10^{-7} in the infrared. This ratio depends on many factors: the semi-major axis, the planet's mass and composition (bond albedo), age, radius and wavelenght (geometric albedo α)

$$\frac{f_p(\alpha, \lambda)}{f_s(\lambda)} = p(\lambda)\frac{R_p}{a}g(\alpha) \tag{2.1}$$

where $g(\alpha)$ is a phase function describing the light path after the reflection.

The observable of the Direct Imaging method are: the orbital elements, the flux (intensity and polarization), temporal variation and, for the planet atmospheres, biosignature.

Figure 2.1: 2m1207 b: the first Direct Imaging Image ever. It was obtained with NACO@VLT in 2004 [8]

2.1.1 Adaptive Optics and High Contrast Imaging

The earth-based instrumentation is strongly limited by the atmosphere.

The light coming by a point-like source light at infinite distance is assumed to be a plane wavefront when it reaches the upper part of the Earth atmosphere. The wavefront encounters atmospheric bubbles with linear length r_0 (Fried parameter). In these bubbles the atmosphere is characterized by costant thermodinamic parameters (temperature, pressure and so on).

If the entrance pupil is smaller then the Fried parameter the effects on the wavefront is the Tip-Tilt (TT), otherwise the High Order effect (HO) [fig: 2.2].

The correction for these elements is given by the Adaptive Optics. The Wavefront Sensor (WFS), the Deformable Mirrors (DM) and the Real Time PC [fig:2.3] are the three main elements in an Adaptive Optics (AO) module.

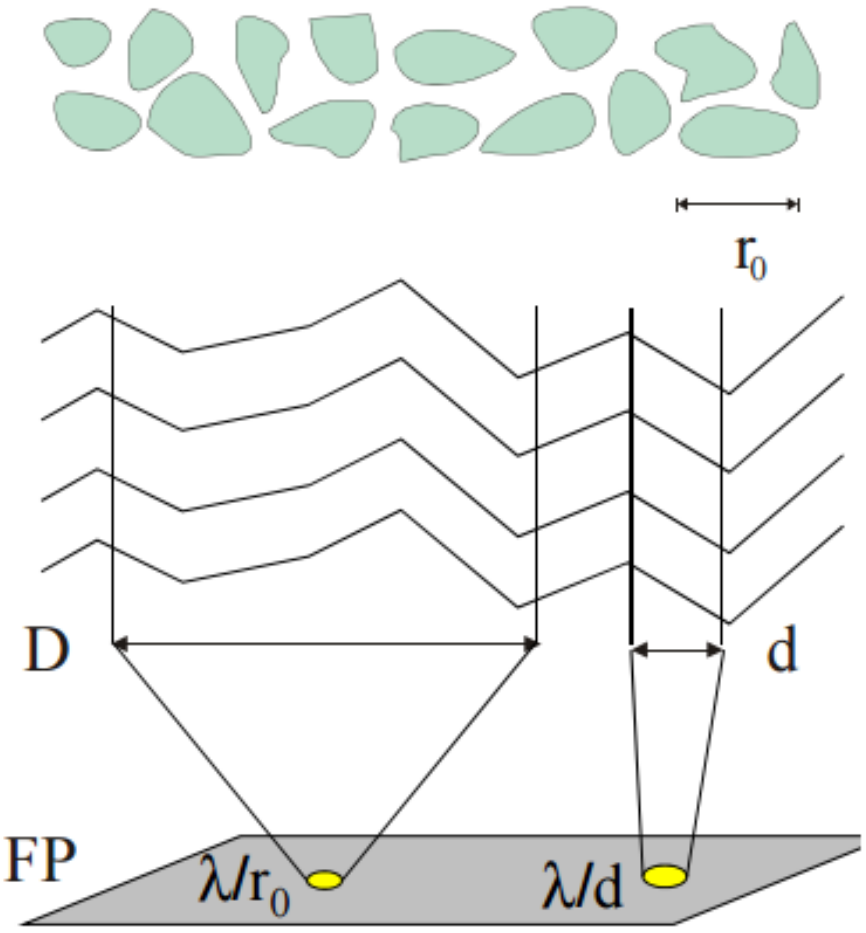

Figure 2.2: Schematic illustration of the TT and HO effects on the wavefront [9]

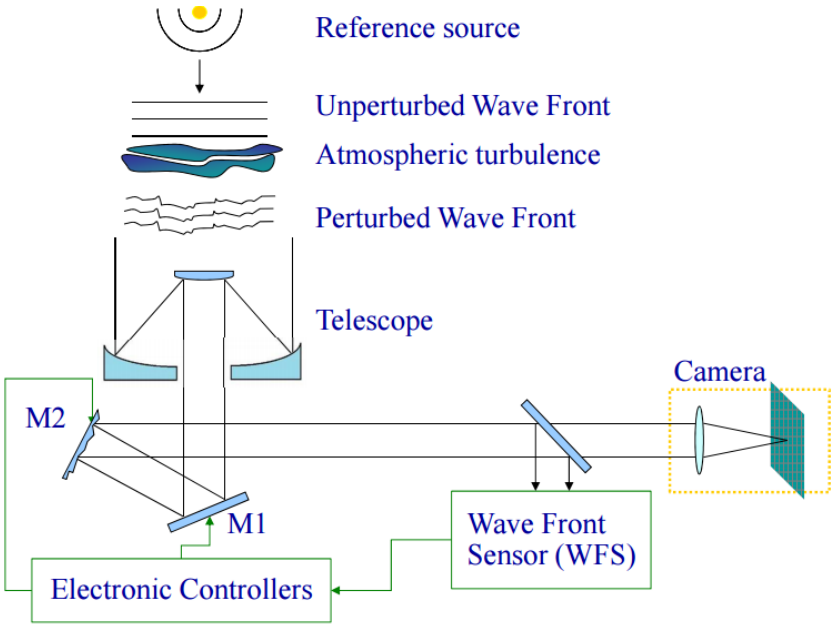

Figure 2.3: Schematic illustration of the AO: the signal pass from the WFS to the electronic devices (which includes the Real Time PC), that send the signal back to the DM. In this way there is a loop for the correction of WF [9]

The typical used WFSs are the Shark-Hartmann, the curvature and the pyramid [fig:2.4], while regarding the deformable mirrors there are a lot of types, but the piezo-electric is the most common one.

The main limit of the classical adaptive optics is the size of the corrected field of view (FoV). The light coming from the science target and the reference star goes through slightly different cylinders of atmosphere before reaching the telescope entrance pupil and undergo different distortions, mainly when very high strong turbulent layers are present. This effect is called angular anisoplanatism. Because of this limitation, the reference object is required to be very close to the science target. Of course the smaller the corrected FoV, more difficult to find a suitable reference. For this issue there are two possible orientation: the Natural guide star (NGS) (typically used for the AO) and Laser guide star (LGS) (typically used when there are no plausible near bright stars, and so an "artificial" one is created. On the other hand, once it's chosen the orientation, it's time for the layer: in some cases (location with low ground atmospheric perturbation) are used the Ground Layer Telescopes, where it's needed more then one reference star: in this way it's talked about Multi-conjugate adaptive optics.

In optical and infrared astronomy, High-Contrast Imaging observations are defined as any observation requiring a technique to reveal a celestial object of interest that is in such close angular proximity to another source, which should be brighter by a factor of at least 10^5. That optical effects hinder or prevent the collection of photons directly from the considered object and its light due to scattering or diffraction, which would

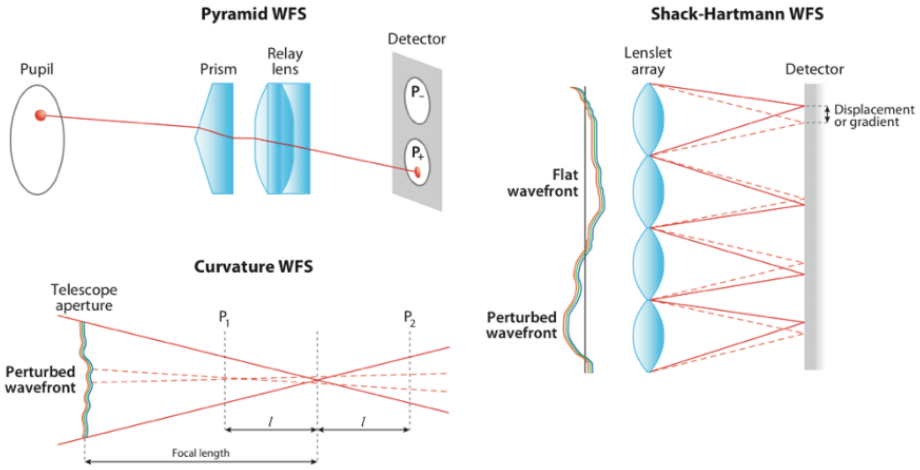

Figure 2.4: Schematic illustration of the WFS [9]

prevent the observation without special conditions or methods to suppress its light. This tecnique has two principal scientific goals: the first is the planets comparison and the second is the study of planet formation.

The five most important parameters for High Contrast Imaging (HCI) are: the contrast, the IWA (inner work angle), the OWA (outer work angle), the planet troughtput and the chromatism.

The IWA is th inner boundary of high-contrast search area (which is the limitation given by the coronagraph mask as it will be seen) and the OWA is the outer boundary of high-contrast search area [fig:2.5]. The planet troughtput is the light fraction of the planet that survive to the suppression due to the coronagraph. The useful troughput for the observation is showed in [fig:2.5], the one fraction of light which go into the detector The chromatism is the capacity of the coronagraph to suppress light on a large range of wavelength. Low chromaticity is better for the characterization of both planets and protoplanetary disks.

In the matter of protoplanetary disks, the HCI can reveal their architecture, that must have previously been determined by fitting the IR excess in a spectrum of the system. This can be done by estimating the extent of flaring, the presence of holes or gaps, and the temperature distribution through the disk. High-contrast imaging of disks in the optical and near-IR can reveal physical parameters that are either difficult to obtain or are hopelessly degenerate with other parameters. For instance, high angular resolution imaging reveals disk radius, inclination, and asymmetries. High-contrast imaging also allows the observer to study the light being scattered from dust particles in a circumstellar disk. In particular, multiwavelength observations of disks probe different depths in the disk, because the dust opacity is highly wavelength dependent. Longer wavelength imaging probes closer to the midplane of the disk, where the density of larger particles is higher due to settling. Also, by studying the distribution of the scattered light in a circumstellar disk, the observer can gain clues to the nature of

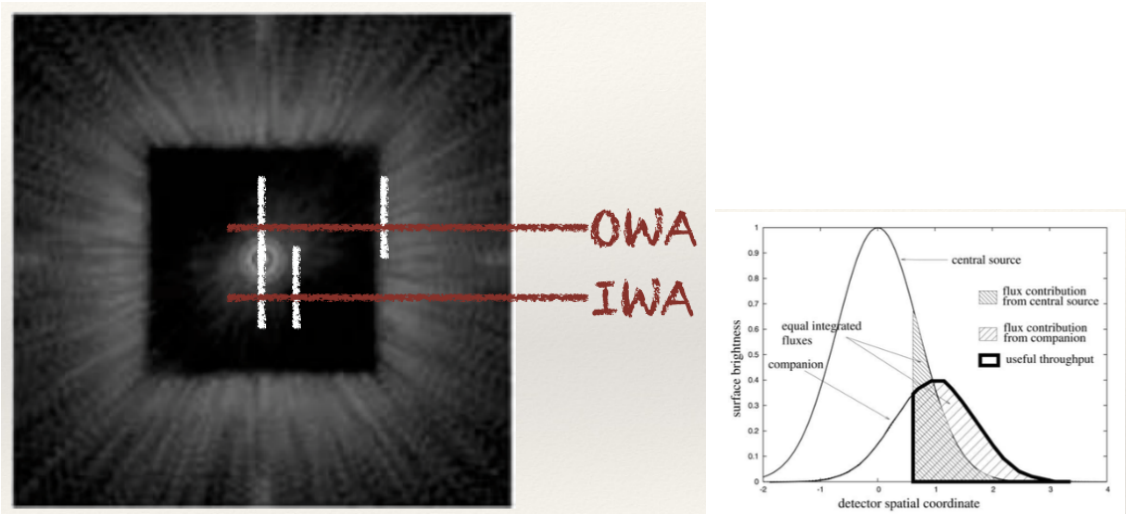

Figure 2.5: In the first image the schematic illustration of the working angles [14]. In the second one there is the planet troughtput from the star to the planet. The useful troughtput is the fraction of light that is seen in the detector [17]

the scattering phase function (see later in the coronagraph section) and, hence, make inferences about the size of the dust grains. Studying the scattering properties in this way can directly address how dust grains grow within the disk. There was also some high-contrast observational programs that have detected disk asymmetries: evidence for interaction between a companion and a disk (e.g., Kalas, Graham & Klampin 2005; Oppenheimer et al. 2008)

On a technical point of view, the High Contrast Imaging is a combination of Adaptive optics, Speckle Suppression and the use of the Coronagraph. In this way the atmosphere (and Speckles) and the diffraction are "erased': the image is now prepared. Let's see the uses and types of the coronagraph and the mechanism of speckle supression.

The concept for HCI observations is displayed in [fig: 2.6]. The coronograph element will be described ahead.

Coronagraph

The point-spread function (PSF) of a telescope equipped with Adaptive Optics typically consists of a bright diffraction-limited core, with several Airy rings superimposed on a wide scattered light halo containing several percent of the total flux. The improved image quality provides access to a region within a few times the telescope' s diffraction width, with the dynamic range limited by the stellar halo and the bright Airy rings, rather than by atmospheric seeing. Further significant enhancement in contrast can be achieved by suppressing the noise associated with the stellar light by rejecting it from the area of interest in the focal plane. The technique, employing some form of mask

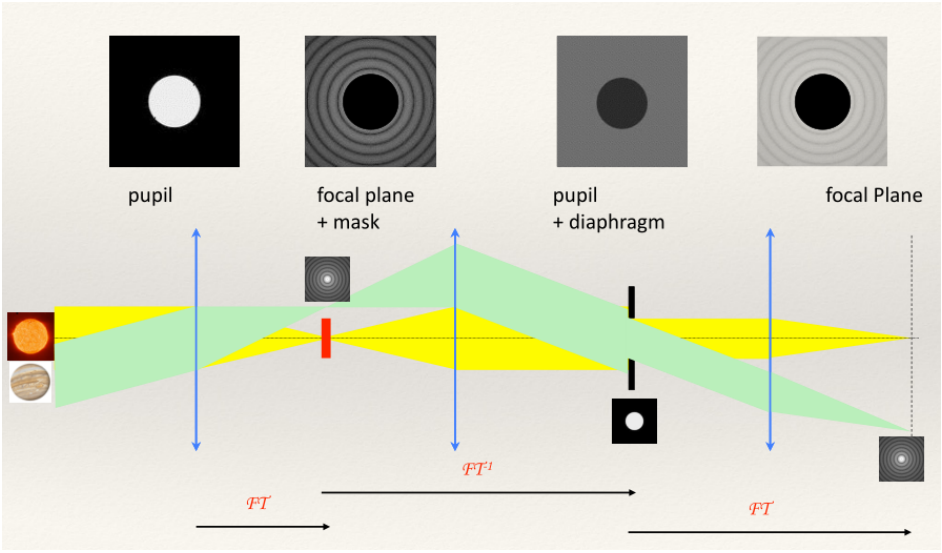

Figure 2.6: Schematic illustration of the coronagraphy for the planets imaging: with the removal of the disk section of the star, it's possible to detect the planet's light [14]

in the telescope focal plane, is referred to as coronagraphy, after its early development to observe the solar corona.

The first sperimented coronagraph was a Lyot one, which used an amplitude mask, physically blocking the central stellar light. Recent coronagraphs also employ phase masks to cancel light through self-interference.

As a result, the combination of a coronagraph with an adaptive optics system aims to block the core of the image of an on-axis point source, suppress the bright diffraction rings and halo, remove light that would otherwise reduce the dynamic range, and improve the prospects of imaging faint off-axis structure.There are also cases in which there is no used adaptive optics (e.g. Golimowski et al.,1992; Nakajima et al., 1995).

Ideally, a coronagraph coupled to an Adaptive Optics system would perform as if placed above the atmosphere. The image of a point source in the image plane would be a pure Airy disk, and the size of the Lyot stop could be chosen using Fourier theory. The Lyot Stop must also be optimised for a given telescope according to specific atmospheric conditions. For a perfect coronagraph, and an entrance pupil with no phase aberrations,there would be zero light outside of some specified angle. In practice two effects limit the efficiency of all coronagraphs in the imaging of object in which the host stars are point-like sources and the images are dominated by diffraction: residual effects due to imperfect atmospheric correction, and imperfect optics.

An important tecnique used on coronagraphy science is the Apodisation, that removes "the foot of the PSF": in a pratical manner it works as a filter, used to remove the Airy disks in the image, giving a better focus of the image and necessary in High Contrast Imaging. Its effect on the image can be seen in a HCI observation [fig: 2.7].

It applies in different ways, cause it depends by the amount of light is needed to erase in a typical configuration of the telescope.

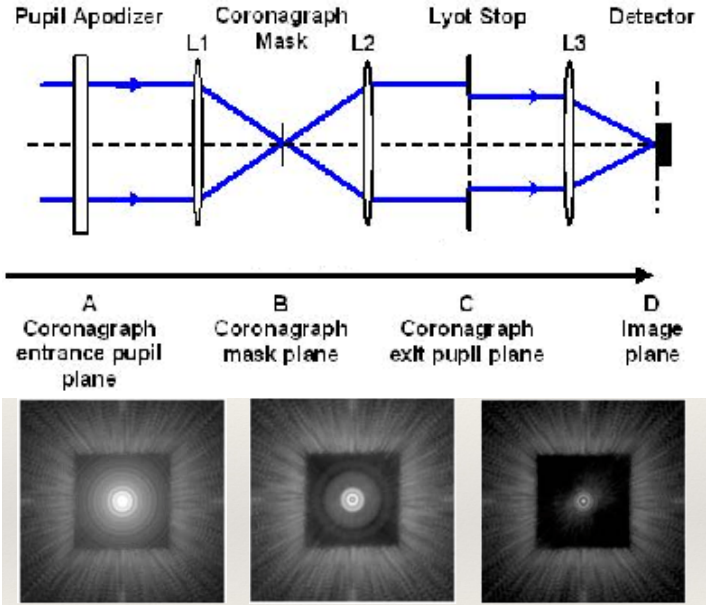

Figure 2.7: The first image is a schematic illustration of the Apolized Lyot Coronagraph. The Coronagraph is a simple Lyot without the pupil apodaizer. The second one is the concept of apodization: the external Airy disks became more darkened [14]

As of today there are different concept of Coronagraphs, that will be only explained in short:

- Interferometric coronagraphs [14]: akin to nulling interferometers, this class relies on interferometric combination of discrete beams derived from the entrance pupil. Examples include the achromatic interferometric coronagraph,which uses a beam splitter to destructively combine two copies of the entrance pupil, one of them π-phase shifted and flipped.

- Pupil apodisation coronagraphs [18]: these designs are all characterised by a modification of the pupil complex amplitude, yielding a point-spread function suitable for high-contrast imaging. Apodisation can be performed by a pupil plane amplitude mask which can be continuous or binary, or by a phase mask. A classical concept of this coronagraph can be found on [fig: 2.7].

- Improved Lyot coronagraphs with amplitude masks [14]: improved performance of the basic Lyot design can be obtained by better matching the Lyot stop to the light distribution in the reimaged pupil. It can be done emulating the Apolyzed Lyot as in the image.

- Improved Lyot coronagraphs with phase masks [14]: a phase mask can be used to introduce phase shifts in the focal plane to create self-destructive interference, rather than employing an opaque disk to block the stellar light

It is necessary to include a little explanation on what is the purpose of a 4-quadrant phase mask. The effect of the wavefront mean tip-tilt consists in a shift of the focalized spot on the focal plane, where the phase mask will be inserted [fig: 2.8].

The mentioned shift translate into a signal, that can be seen as, if the shift is on the x-axis, $S_x = \frac{(B+D)-(A+C)}{(A+B+C+D)}$ and on the y-axis, $S_y = \frac{(B+D)-(A+C)}{(A+B+C+D)}$. The 4-quadrant phase mask concept and its shift concept can be seen in [fig: 2.8]

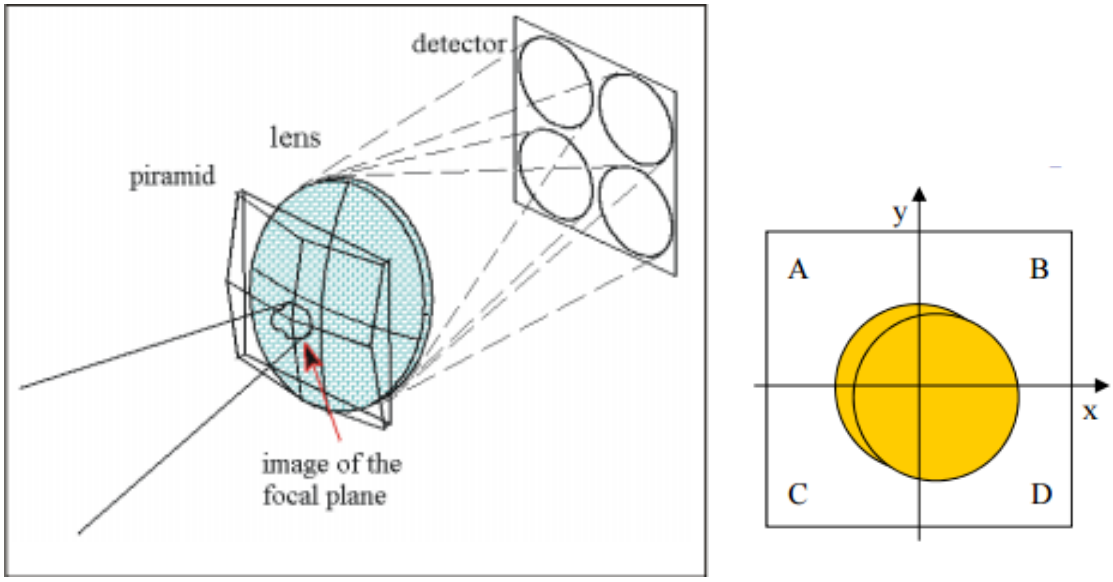

Figure 2.8: Illustration of the 4 quadrant concept and the concept of the shift behaviour on the focal plane [9]

The focal plane is divided into four equal area quadrants, centred on the optical axis.

A π-phase shift is applied to opposing quadrants, which results in destructive interference for a bright star located at its geometric centre. A Lyot stop is placed in the exit pupil to remove diffracted starlight, as in the original Lyot coronagraph. Implementation is based on the precision mounting of four half-wave plates (Riaud et al., 2003). In practice, implementation of the π-phase shift tends to introduce chromatic terms, while the phase transitions between adjacent quadrants introduces large dead zones. In this way it's obtained a smaller IWA, but the aligment is crucial and there is a dependence on the wavelenght.

Speckles Suppression

The other necessary tecnique required for working in High Contrast Imaging is the Speckle Suppression. A speckle is defined as the result of both destructive and costructive interferences that have a casual phase. The result is on the image [fig: 2.9]

There are various method in which is possible to eliminate the speckles. There will be mentioned some of them:

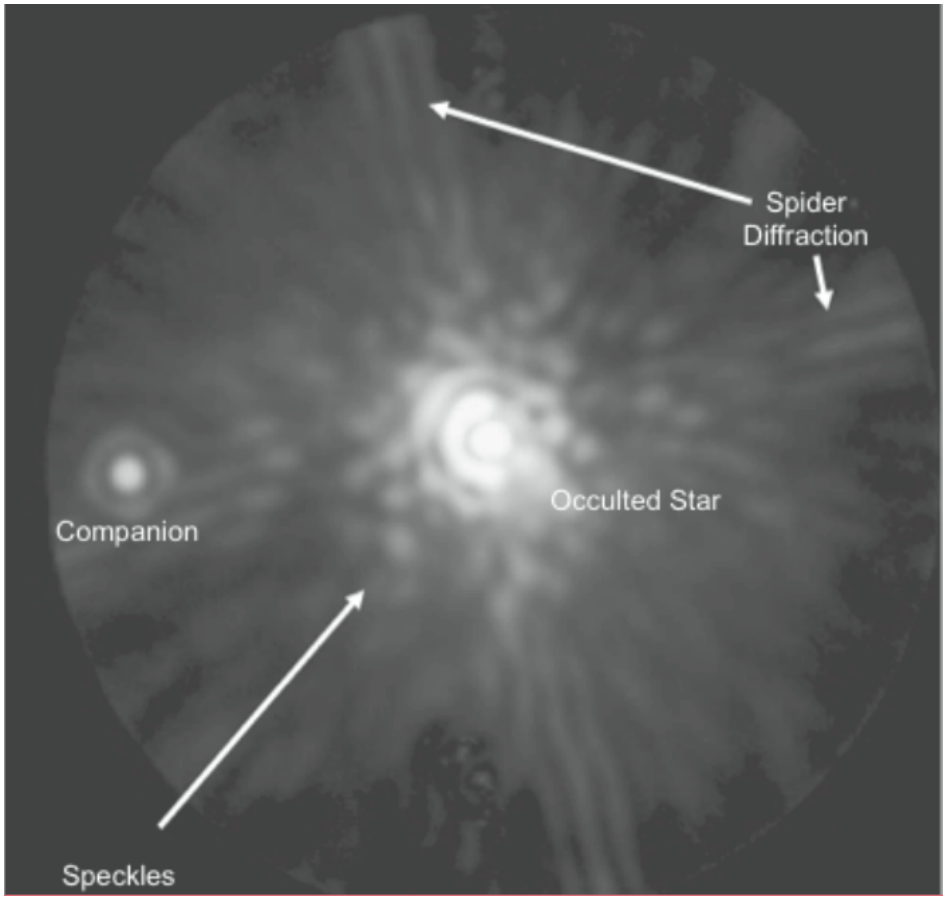

Figure 2.9: An image that enanches the speckle problem for the planets's detectability: if the planet was near the star, it could be hidden by the speckles [14]

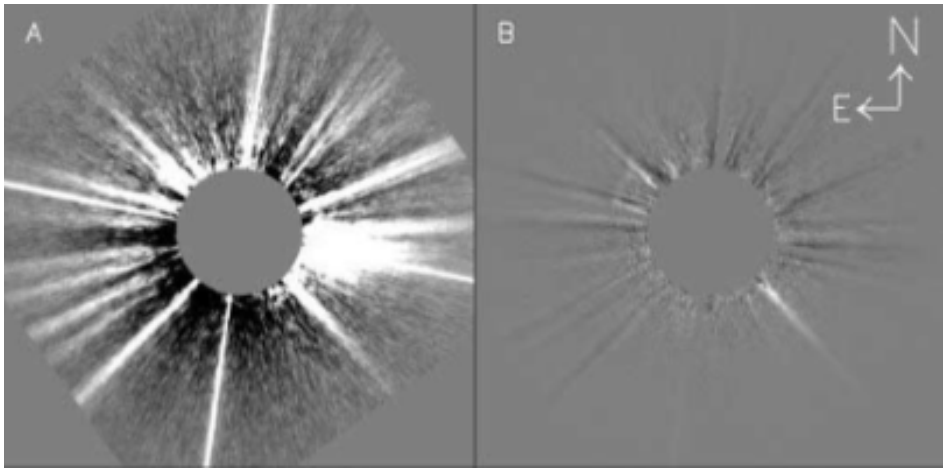

Figure 2.10: ADI result from a high contrast image into the speckle suppressed one [14]

- Interferometric subtraction [15]: it makes use of the fact that, unlike the light from the nearby companion, speckles arising from the light of the central source are coherent with it, whether the speckles are evolving more rapidly as on the ground, or are essentially stationary as in space.

- Angular differential imaging (ADI) [28]: it is derived by the fact that observations have shown for integrations longer than a few minutes, then the PSF (Point Source Function) noise converges to a quasistatic noise pattern, thus preventing a gain with increasing integration time. It is thus necessary to subtract the quasistatic noise using a reference PSF, which is obtained by the images taken while the instrument rotate slowly with time around the star. The quasistatic noise subtracts the original PSF. In this case the observer must be beware of the possibility that the object's trace can be erased during this process that can be evaded by keeping the telescope pupil fixed on the science camera. The final result of this application is observed in the image [fig: 2.10]

- Spectral differential imaging [12]: it aims to suppress the speckle pattern by isolating light from a strong absorption or emission feature. As an example the spectra of cool planets are thought to be dominated by strong methane bands, so the planet image will be absent (or present) in two or more adjacent bands in (or out) that bands. In the end by differentiating the images of the two outcomes the planet could get out of it.

- Psf subtraction [14]: uses a reference object in condition as similar as possible to the target object. They are then put in a common intensity and finally subtracted.

- Speckle deconvolution [13]: it is applicable when the planet image does not extend over the whole observed spectrum. The object can be later "extracted" using the data cube.

Figure 2.11: Project 1640 logo [19]

- Polarimetric differential imaging [16]: it's made the assumption that the speckle are indipendent of polarization. If that's true then the telescope it's used in a polarization mode observation and then used to locate the planet by differentation.

2.2 Project 1640

Project 1640 conducts remote reconnaissance of planetary systems around stars other than the Sun.

Specifically it is designed to image planets orbiting nearby stars and to acquire low-resolution spectra of them simultaneously. It is currently one of the most advanced and highest contrast imaging system in the world and was successfully installed at the Palomar 200-inch telescope July 2008, with a major upgrade and additional control systems added by June 2012.

Observations at Palomar were on-going for a 3-year survey of some 200 nearby stars to find any type of object orbiting them. The primary goal is comparative spectroscopy of young, warm giant planets around these stars, to understand the range of planets extant, and how they form and evolve.

The combination of an extreme adaptive optics system, an advanced coronagraph and hyperspectral imager, and a unique wavefront sensor calibration unit, allows for the detection of objects up to ten-million times fainter than a star within a field of view of 4 *arcsec*.

The goal of Project 1640 is to acquire spectral and orbital information for as many

exoplanets and brown dwarfs orbiting nearby stars as possible, to aid in the development of a comprehensive theory of planet evolution and diversity.

2.2.1 Specifical Science of Project 1640

There are particular cases of interest in this project, which are summaried here in order to understand its goal on a more scientifical point of view[19].

Circumstellar disks

Understanding the connection between circumstellar disks and planets is crucial for a complete picture of planet formation. The first few million years of planet formation involves a competition between planetary accretion and gradual clearing of the disk, as gas-rich protoplanetary disks transition into full-fledged planetary systems with gas-poor disks. Does this allow enough time for the accretion of planetary cores and subsequent rapid accumulation of massive gas envelopes, which is the process generally thought to build gas giants? Or does gas giant formation proceed from gravitational disk instability, which seems to require only a few hundred years? Observing a statistically significant number of systems having both young gas giants and circumstellar disks could tell us whether core accretion or disk instability, or some combination of the two processes is the more probable scenario. This is stricly connected to the study of young planetary system.

Young planetary systems

They are likely to harbor not only planets but also left over material from early stages of planet formation, like asteroid belts and comet reservoirs, which can be traced by the dust produced in collisions between their rocky constituents. Many such circumstellar debris disks have been detected by IRAS and Spitzer from observing mid- and far-infrared emission of heated dust grains, and follow up observations of nearby disks by the Hubble Space Telescope have spatially resolved some of these disks in scattered optical and near-infrared light. Because Project 1640 has a sensitivity much higher than Hubble's NICMOS instrument, it will be able to image faint debris disks, mapping morphological features like spirals, warps, offsets, gaps, or other asymmetries that could imply interaction with unseen planets. It will also allow us to obtain spatially resolved, low resolution near-infrared spectra of bright nearby debris disks, giving us information on grain composition and size distributions of particles, as well as how water is distributed at radial distances from a few to 100 AU. In addition, the age of observed systems covers the important period in the evolution of our Solar System known as the late-heavy bombardment, and could have implications for the possible emergence of life.

Figure 2.12: Gemini Southern Observatory

Evolved stars

Although not currently included in the sample of stars selected for our survey, evolved stars and their circumstellar envelopes could be successfully observed with a high-contrast imaging instrument like Project 1640. As stars enter the last stages of evolution before they decay into stellar remnants, dust and gas are spewed into the interstellar medium. Exactly how stars do this remains poorly understood. Project 1640 can study this process in detail, estimating mass-loss rates and looking for arcs, elongated and bipolar structures, spirals, clumps, etc. Imaging detached shells around evolved stars could possibly give ages and formation time-scales which could be compared to various theories.

2.3 GPI

GPI is the acronimus for Gemini Planet Imager. It is in the Gemini Observatory, which consists of a twin 8.1-meter diameter optical and infrared telescopes located on two of the possible best observing sites on the planet [fig: 2.12]. From their locations on mountains in Hawaii and Chile, Gemini Observatory's telescopes can collectively access the entire sky.

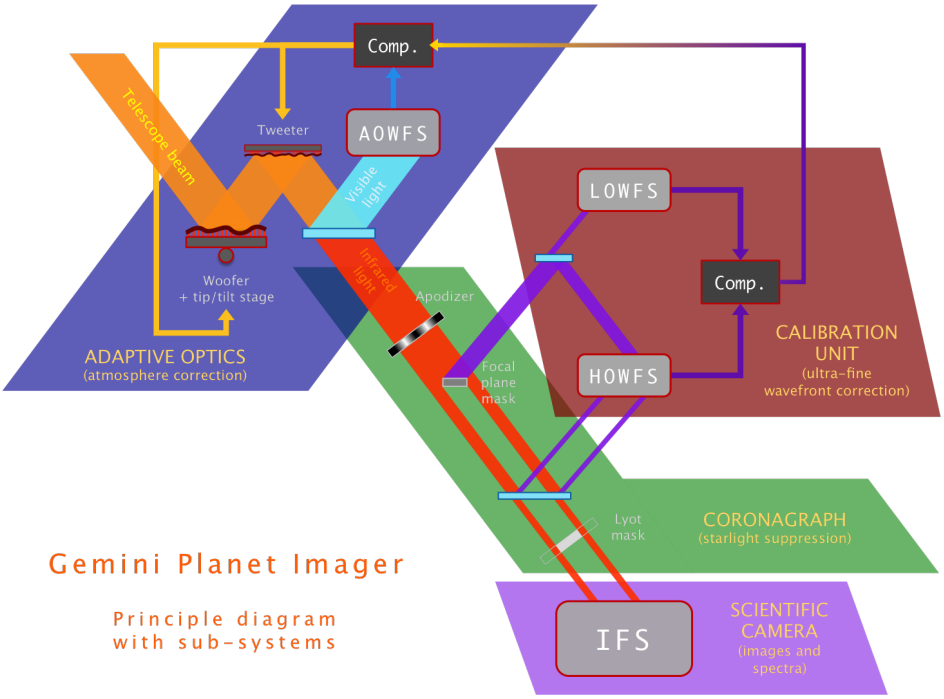

Figure 2.13: Schematic illustration of the GPI camera. The calibration unit divides the limiting magnitudes with the AOWFS (I-band), the LOWFS (H-band). It should be noted that it is not possible to observe without the AOWFS and Coronagraphic modes are not possible to observe without the LOWFS. Finally the HOWFS detect the High orders and provides to correct them [20]

2.3.1 Instrument Description

The instrumentation of the Gemini facilities has, in the northen facility, GMOS and GRACES for visible observation, NIRI, NIFS, GNIRS and TEXES (TBA[1]) for the IR and for the AO and calibration system ALTAIR and GCAL, while the southern facility has GMOS and DSII/speckle (TBA) for visible observation, GSAOI, GPI, FLAMINGOS-2 and Phoenix (TBA) for the IR and GCAL and Gems for the calibration system and AO. In this section will be only described GPI, the high contrast imager.

GPI [fig:2.13] is an extreme adaptive-optics imaging polarimeter/integral-field spectrometer, which will provide diffraction-limited data between $0.9-2.4\ \mu m$. The system will provide contrast ratios of 10^6 on companions at separations of $0.2-1\ arcsec$ in a $1-2\ h$ observation. The science instrument will provide spectroscopy or dual-beam polarimetry of any object in the field of view. Bright natural guide stars ($I \ll 9\ mag$) are required for optimal performance of the GPI adaptive optics system. GPI will be capable of detecting point sources down to $H = 20\ mag$, with precision $\geq 5\sigma$, in $1\ h$ (absent photon noise from a bright companion). GPI combines four main optomechanical systems:

[1]to be announced

- The adaptive optics (AO) system, responsible for fast measurement of the instantaneous wave front, and for providing wave front control via two deformable mirrors.

- The calibration unit (CAL) is a high-accuracy infrared wave front sensor tightly integrated with the coronagraph. It provides precise and accurate measurements of the time-averaged wave front at the science wavelength and coronagraph focal plane, to suppress persistent speckles caused by quasi-static wave front errors in the final image. It also provides pointing and focus sensing to keep the target star centered on the coronagraph with 1 *mas* accuracy and slow low to high-order aberration corrections.

- The coronagraph uses a combination of apodized masks and focal-plane stops to control diffraction and pinned speckles.

- The integral field spectrograph produces the final science image, including simultaneous multiple channels to suppress residual speckle noise in the spectroscopy mode or polarimetric imaging allowing the determination of the four Stokes parameters. [25]

2.3.2 Observation Modes

The GPI instrument control software uses observing modes to specify sets of instrument optical masks that work together. Each mode consists of a unique set of 4 elements: Filter, Apodizer, Focal plane mask, Lyot Mask. Observation modes come in several basic flavors:

- Coronagraphic observations, most common for GPI.

- Direct observations, with no coronagraphic masks in use.

- Unblocked (unocculted) observations, which use the coronagraphic Apodizer and Lyot mask but not the focal plane masks. These are occasionally used, mostly for certain types of calibration observation

- NRM modes for non-redundant mask interferometry and a single Dark mode for detector calibrations.

The primary user configuration decision is over the coronagraph focal plane stop and pupil mask, the observing wavelength (Y, J, H or one of two filters in the K band) and the desired contrast and inner working distance (size of the Coronagraphic mask). Coronagraph configurations are: direct imaging (for imaging or polarimetric imaging), Coronagraphic (combined with either polarimetric imaging, or spectroscopy). GPI will automatically select appropriate apodizer, focal plane masks, and Lyot stops for each wavelength. In GPI's apodized-pupil Lyot coronagraph, these three are carefully matched to each other - performance would be severely degraded if e.g. the Y-band focal plane mask was used at K band.[20]

Direct imaging (without coronagraph) or NRM (Non Redudant Mask) are available options for all filters. Each individual spectrum is 12-18 pixels long. The coronagraph mask diameter sets a hard limit on the inner working angle, but typically full performance is only achieved $\sim 1\frac{\lambda}{D}$ beyond the mask radius; the contrast curves are tabulated and should be used to predict performance at a given radius. In addition, coronagraph masks are available for a non-redundant aperture masking mode (namely NRM-modes), at the moment we have no performance data for the NRM-modes. It should also be noted that the GPI pipeline at the moment will not reduce fully the NRM data. Any NRM data are only guaranteed to be taken under the requested conditions as any other performance indicators are not available. In polarimetric mode, the light is not spectrally dispersed - the whole waveband is split into two polarization channels.

In the direct imaging mode (without coronagraph) the CAL unit is not available. Note that the contrast curves are based on the assumption of the use of a coronagraphic mask.
As for the configuration of the mode in the instrumental part, it must be taken care of:

- Sky Rotation: The masks have fixed orientation and optimized with respect to a fixed Cassegrain angle. With the Cassegrain angle always fixed (and not adjustable) it means that the sky will always rotate around the detector optical axis determined by the OIWFS axis.

- Science Camera Configuration: The IFS science instrument has few moving parts. The basic parameters are operating wavelength (set by filters) and polarimetry mode selection. The science camera incorporates the following mechanisms:

- Filter wheels: Blocking filters are used to isolate diffraction orders and to control the background reaching the detector array. These will closely approximate the standard Y, J, H filters, plus two custom filters (K1 and K2) to span the two-micron window. Filter bandpasses are listed in the tables above, and are shown graphically in the figure below. As stated above, provision of the Y filter is a design goal.

- Polarization analyzer: an optional polarizing beam splitter (a Wollaston prism), introduces an angular deflection between ordinary and extraordinary rays and produces two images with orthogonal polarization states on the focal plane array. Together with an external rotating half-wave plate, the analyzer permits measurement of the Stokes parameters.[20]

2.4 SPHERE

SPHERE [fig: 2.14] (Spectro-Polarimetric High-contrast Exoplanet REsearch) is a commonly called Planet Finder. The main purporse of this instrument is locate, with the most possible highest contrast in a limited field of view and short distances, the planets and the disks.

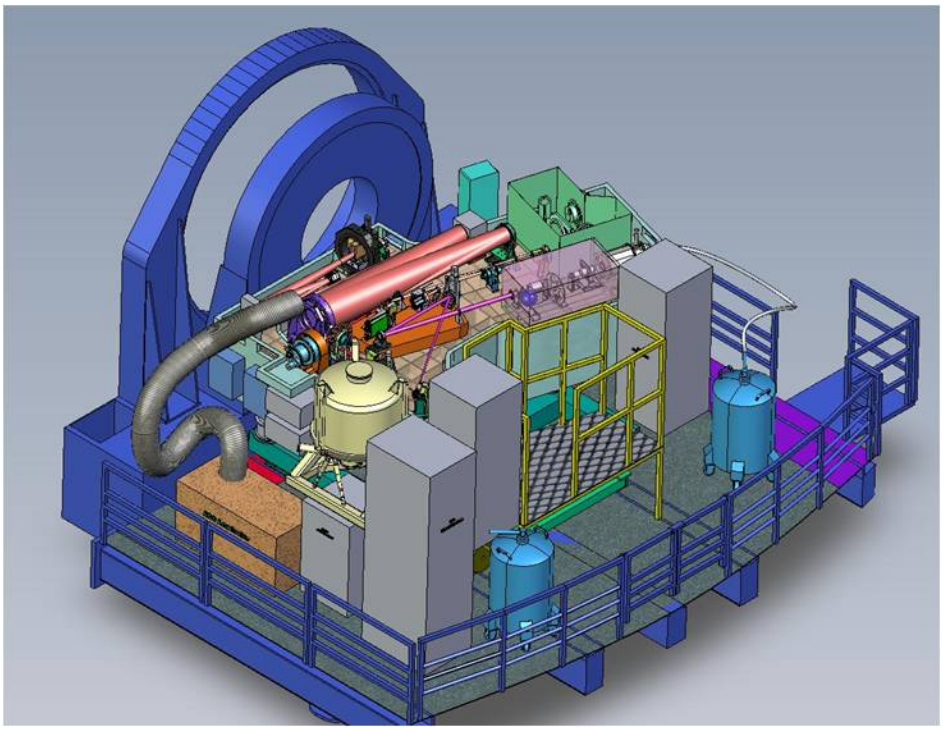

Figure 2.14: SPHERE at VLT

2.4.1 Scientific goal and Target

The primary goal of extra-solar planet science for SPHERE will be a better understanding of the mechanisms of formation and evolution of planetary systems. The fundamental observational parameter is the frequency of objects as a function of mass and separation. Theoretical models of planet formation predict that the peak of formation of giant planets is found close to the snowline, thanks to the availability of a larger amount of condensate in the protoplanetary disk. In outer regions, the longer timescales involved should make planet formation a less efficient process. Migration mechanisms and long term orbit instabilities will alter the original distribution. Even if the radial velocity is the actual best and efficent tecnique to reveal exoplanets (along with the transit for space missions), the High-resolution and High-contrast imaging could be the better option for the most distant planets in respect of the star. Also SPHERE is the best instrument to describe the young system (especially the ones with disk). Along with that, it's possible to say that the target classes are linked to particular cases that are difficult with other methods, or not possible:

- Nearby young association (on the order of $10 - 100$ Myr and $30 - 100$ pc as constraint for the survey): this will offer a very good chance to detect low mass planets (rocky planets), since they wil have brighter sub-stellar companions.
- Young active F-K dwarf (with survey constraint within 1 Gyr and distances $\ll 50$ pc): Solar-like cases

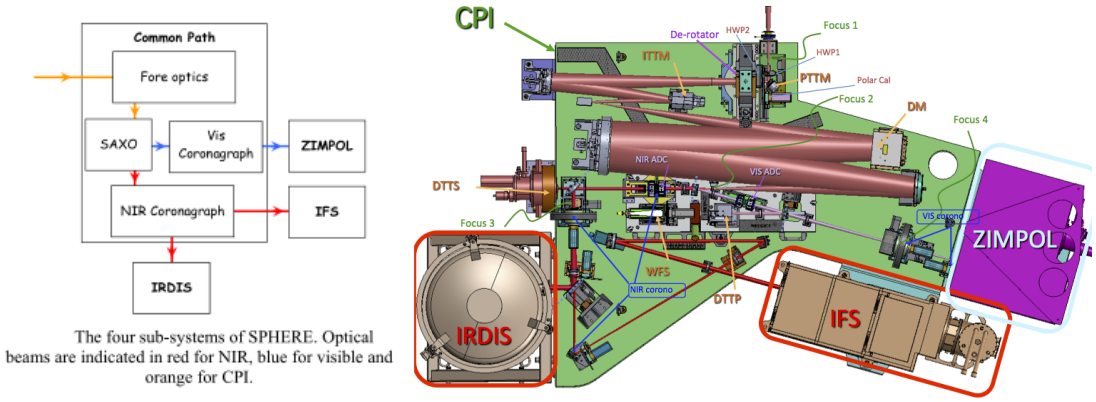

Figure 2.15: Simple and detailed CPI of SPHERE

- Nearest Star (distances $< 20\ pc$): smallest orbits and the only possibilities for detecting planets by directly reflected light.
- Stars with known planets: especially any that exhibit long-term residuals in their radial velocity curves, indicating the possible presence of a more distant planet
- Young early type stars
- Planet candidates from astrometric surveys [21]

2.4.2 Instruments Description

SPHERE is divided into four principal component: CPI (Common Path and Infrastructure), IRDIS (InfraRed Dual Imaging Spectrograph), IFS (Integral Field Spectrograph) and ZIMPOL (Zurich Imaging Polarimeter)

CPI

The Common Path [fig: 2.15] is mounted on a large actively damped optical bench to which each science instrument is docking as whole. Besides classical optical components, the common path components are the high order deformable mirror from CILAS, toroidal mirrors manufactured by spherical polishing of pre-stressed substrates 1 , a dedicated electron multiplying CCD for wavefront sensing, achromatic 4 quadrants coronagraph, classical and apodized Lyot coronagraphs. Also in SPHERE is in using the extreme adaptive optics (SAXO). There are three loops and one off line calibration compose the extreme adaptive optics system. In particular the components are:

- The main AO loop corrects for atmospherics, telescope and common path defects. The main impact is the increase of detection signal to noise ratio through the reduction of the smooth PSF halo due to turbulence effects.

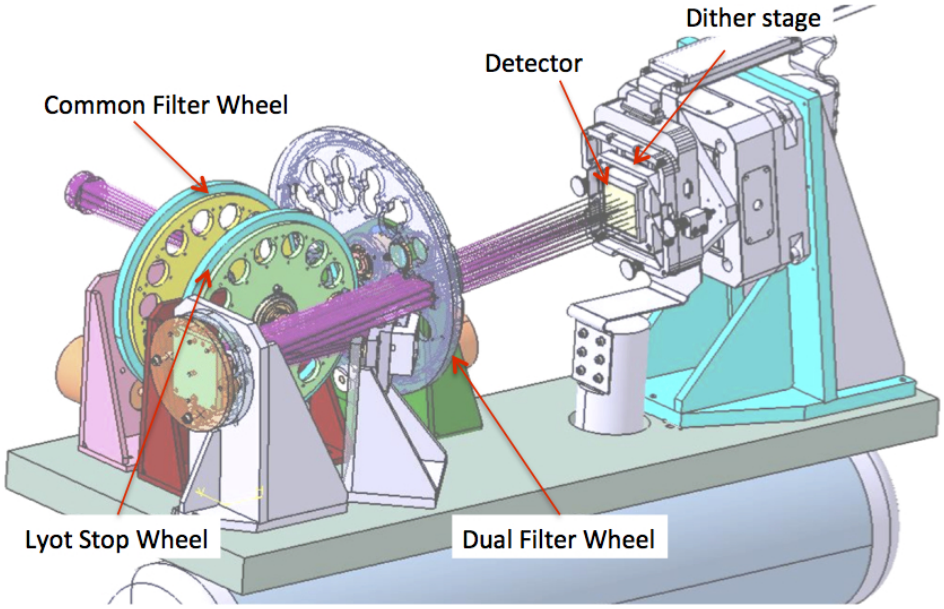

Figure 2.16: IRDIS configuration

- The Differential Tip-Tilt loop ensures a fine centering of the beam on the coronagraphic mask (correction of differential tip-tilt between VIS and IR channel). It will therefore ensure an optimal performance of the coronagraph device.
- The Pupil Tip-Tilt loop corrects for pupil shift (telescope and instrument). It will ensure that the uncorrected instrumental aberrations effects (in the focal plane) will always be located at the same position and thus will be canceled out by a clever post-processing procedure.
- Non-Common Path Aberrations will be measured with phase diversity, and their pre-compensation will lead to the reduction of persistent speckle. [21]

IRDIS

The IRDIS science module [fig: 2.16] covers a spectral range from $0.95-2.32\ \mu m$ with an image scale of 12.25 mas consistent with Nyquist sampling at 950 nm. The field of view is 11 x 12.5 $arcsec$, both for direct and dual imaging. In addition to these modes, long-slit spectroscopy (LSS) at resolving powers of 50 and 500 is provided, as well as a dual polarimetric imaging (DPI) mode. Two dispersion devices are provided, a double prism for low resolution (LRS, $R \sim 50$) and a grism for medium resolution (MRS, $R \sim 500$). The main challenge of IRDIS is to achieve less than $10nm$ differential aberrations between the two channels. An error budget based on high-quality polishing technology satisfies the requirement, and prototyping of DBI filters confirmed this budget. The beam-splitter option has been favored because it eliminates spectral blurring problems, which would limit the useful field of view, and allows the use of high-quality materials with high homogeneity in respect of other possible options.[23]

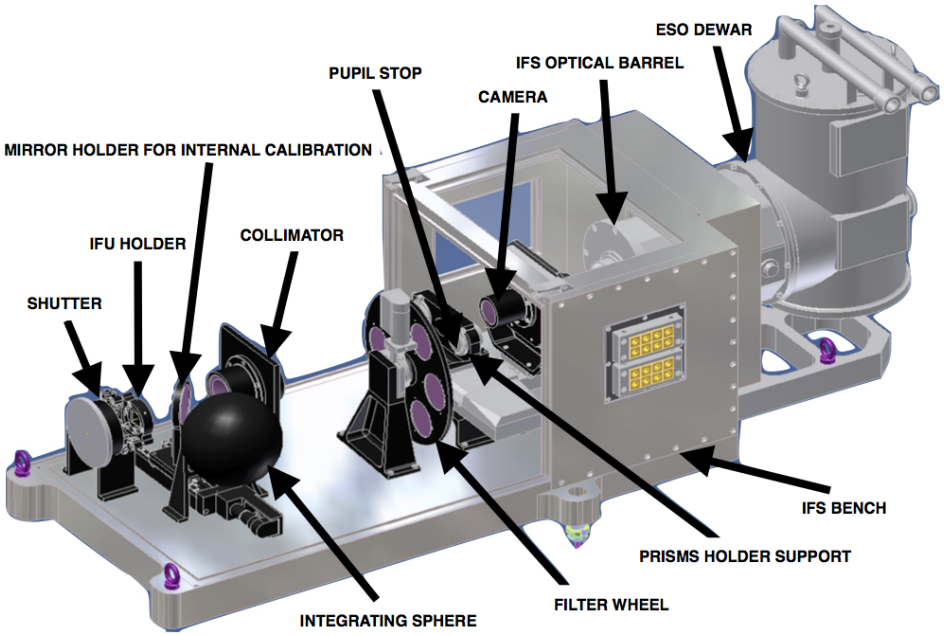

Figure 2.17: IFS configuration

IFS

IFS [fig: 2.17] are very versatile instruments and are perfect for the exoplanetary research. The main advantage of IFS is that differential aberrations can be kept at a very low level; this is true in particular for lenslet based systems, where the optical paths of light of different wavelength within the IFS itself can be extremely close to each other. Additionally, IFS provide wide flexibility in the selection of the wavelength channels or differential imaging, and the possibility to perform spectral subtraction, which in principle allows recovering full information on the planet spectra. The main drawback of IFS is that they require a large number of pixel, resulting in a limitation in the field of view, which is more severe for lenslet-based systems like the IFU.

The BIGRE concept was selected for the SPHERE's IFS. It is based on a lenset array and a second lenslet array allows formation of pseudo-slit images corresponding to a very small portion of the field, which are then imaged on the detector after being dispersed. The main advantage of the BIGRE concept is that the pseudo-slit images are only very mildly dependent on wavelength and have a very good profile and also allows a better control of diffraction effects and a much lower level of cross-talk. Achievement of specifications of the BIGRE concept was proven with a laboratory prototype at INAF-OAPD.[24]

ZIMPOL

ZIMPOL[fig: 2.18] is located behind SPHERE visible coronagraph. Among its main specifications are a bandwidth of $600 - 900$ nm and an instantaneous field of view of 3 x 3 *arcsec* with access to a total field of view of 8 *arcsec* diameter by an internal

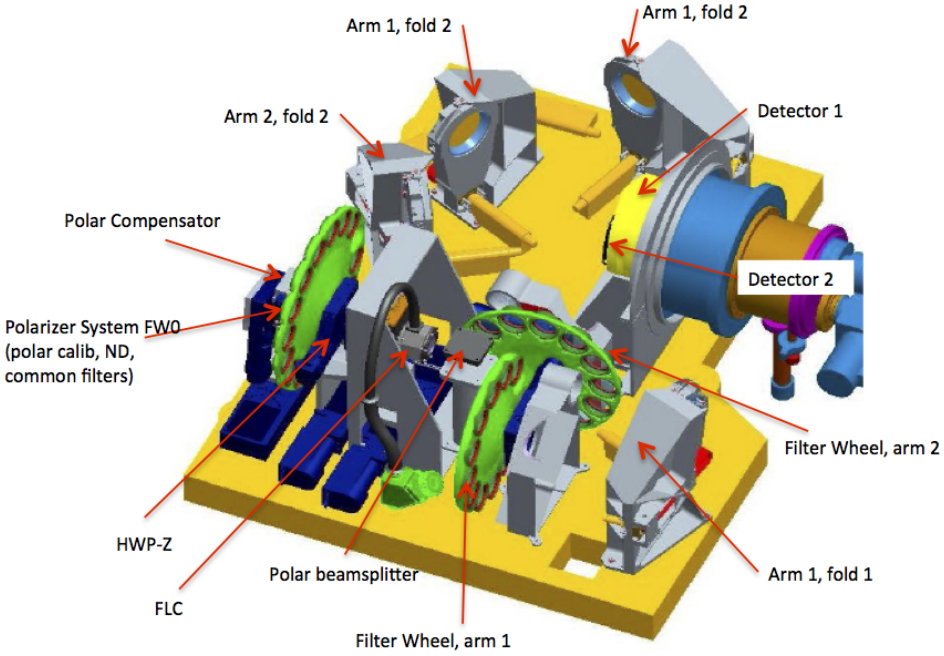

Figure 2.18: ZIMPOL configuration

field selector. The ZIMPOL optical train contains a common optical path that is split with the aid of a polarizing beam splitter in two optical arms and each arm has its own detector. The common path contains components in both arms like calibration components, filters, a rotatable half wave plate and a ferroelectric liquid crystal polarization modulator. The two arms have the ability to measure simultaneously the two complementary polarization states in the same or in distinct filters. The images on both ZIMPOL detectors are Nyquist sampled at 600 nm.

The basic ZIMPOL principle for high-precision polarization measurements includes a fast polarization modulator with a modulation frequency in the kHz range, combined with an imaging photometer that demodulates the intensity signal in synchronism with the polarization modulation. The polarization modulator and the associated polarizer convert the degree of polarization signal into a fractional modulation of the intensity signal, which is measured in a demodulating detector system by a differential intensity measurement between the two modulator states. Each active pixel measures both the high and the low states of the intensity modulation and dividing the differential signal by the average signal eliminates essentially all gain changes, notably changes of atmospheric transparency or electronic gain drifts

2.4.3 Observational Modes

The NIR survey mode is the main observing mode which is used for ~ 80 percent of the observing time. It combines IRDIS dual imaging in H band with imaging spectroscopy using the IFS in the Y-J bands. This configuration permits to benefit simultaneously from the optimal capacities of both dual imaging over a large field (out to ~ 5 arcsec

radius) and spectral imaging in the inner region (out to at least 0.7 *arcsec* radius). In particular, it allows to reduce the number of false alarms and to confirm potential detections obtained in one channel by data from the other channel. This is a definitive advantage in case of detections very close to the limits of the system. The NIR characterization mode, in which IRDIS is used alone in its various modes, will allow obtaining observations with a wider FOV in all bands from Y to short-K, either in dual imaging or dual polarimetry, or in classical imaging using a variety of broad and narrow-band filters. This will be especially interesting in order to obtain complementary information on already detected and relatively bright targets (follow-up and/or characterization). Spectroscopic characterization at low or medium resolution will be possible in long-slit mode. Additional science cases also benefit from these observing modes (like disks).

The visible search and characterization mode, will benefit from ZIMPOL polarimetric capacities to provide unique performance in reflected light very close to the star, down to the level required for the first direct detection in the visible of old close-in planets, even if on a relatively small number of targets. ZIMPOL also provides classical imaging in the visible, offering unique high-Strehl performance [22]

Chapter 3

Computational approach to the problem

In so far we have discussed a general view of the theoretical, observational and instrumental point of view of the protoplanetary disk theory. Now it shall be discussed about the stellar systems that will be used in the code. This one, as it will be seen, has two main parts: the Least Square fitting and the Monte Carlo simulation, which will be analyzed in a general way at first. As a data test method, it's used the χ^2_{red}.

The Monte Carlo method it's a must for stellar systems in which the orbit are not totally defined: due to the fact that the direct imaging is a recent tecnique, there are little astrometric data in which long period objects cannot have a completely defined orbit.

In order to analyze the orbital behaviour (and so the characteristics of the star system) in a computational way, this code was implemented. The core of the code was already written in IDL (Interactive Data Language) for the study of HR8799 stellar system (Esposito et al 2013). The code was changed by me as a part of this thesis work, in order to be first more effective for the recent studies on the stellar systems and second to be more adaptable to different stellar system in general.

The approach to the problem will be Keplerian. The dynamics of the stellar system is the only one taken into account, and several effects will be neglected in order to simplify the work, either because of their irrelevance or simply because their negligible contribution.

The code will be used for HR8799, β Pictoris and HD 142527: the first two will be used as a function test for the code, the last one will be used for a specific scientific case.

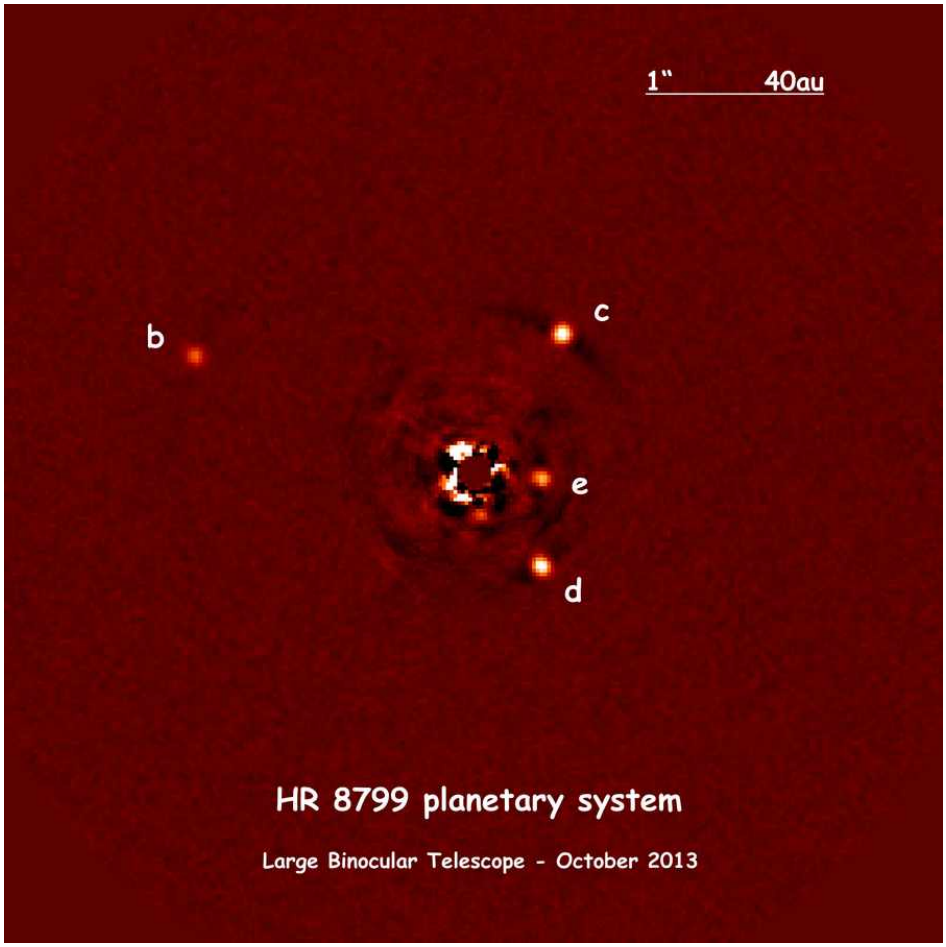

Figure 3.1: An image of HR8799 in High Contrast Imaging in which are visible all the planets [26]

3.1 HR8799, HD142527 and β Pictoris

3.1.1 HR8799

HR 8799 [fig: 3.1] is a young ($\sim 3\ 10^7\ yr$) main-sequence star located 39.55 pc away from Earth in the constellation of Pegasus, with $M_{star} = 1.5\ M_{\odot}$ and $L_{star} = 4.9\ L_{\odot}$. It has a A5V spectral type [27]. It is part of a system that also contains a debris disk and at least four massive planets (even if there are some possibilities of a fifth innermost planet) [28]. Those planets were the first extrasolar planets whose orbital motion was confirmed via direct imaging.

The outer planet orbits inside a dusty disk like the Solar Kuiper belt. It is one of the most massive disks known around any star within 92 pc of Earth, and there is room in the inner system for terrestrial planets. There is an additional debris disk just inside the orbit of the innermost planet.

Because of the inverse square law relating radiation intensity to distance from the source, comparable radiation intensities are present at distances 2.2 times farther from

HR 8799 than from the Sun, meaning that corresponding planets in the solar and HR 8799 systems receive similar amounts of stellar radiation.

A number of studies have used the spectra of HR8799's planets to determine their chemical compositions and constrain their formation scenarios. The first spectroscopic study of planet b (performed at near-infrared wavelengths) detected strong water absorption, which indicates a hydrogen-rich atmosphere. Weak methane and carbon monoxide absorption in this planet's atmosphere was also detected, indicating efficient vertical mixing of the atmosphere and a disequilibrium CO/CH_4 ratio at the photosphere [29]. Compared to models of planetary atmospheres, this first spectrum of planet b is best matched by a model of enhanced metallicity ($\frac{[H]}{[Fe]} = 10\frac{[H]}{[Fe]}_{Sun}$), which may support the notion that this planet formed through core-accretion [29].

Three components of the debris disk were distinguished:

- Warm dust ($T \sim 150\ K$) orbiting within the innermost planet (e). The inner and outer edges of this belt are expected to be close to 4:1 and 2:1 resonances with the planet [28].
- A broad zone of cold dust ($T \sim 45\ K$) with a sharp inner edge orbiting just outside the outermost planet (b). The inner edge of this belt is approximately in 3:2 resonance with this planet, similar to Neptune and the Kuiper belt. A halo of small grains originating in the cold dust component [28].
- The halo is unusual and implies a high level of dynamic activity which is likely due to gravitational stirring by the massive planets. The Spitzer team says that collisions are likely occurring among bodies similar to those in our Kuiper Belt and that the three largest planets (except HR8799e) may not yet have settled into their final, stable orbits [30]

Moreover, there are also some important results on the orbital, observational and dynamical point of view:

- The planetary system is highly packed (4 massive planets in 70 au)
- The dynamical stability at the edge of the system (30 Myr) is difficult to achieve: the system must have planet in a specific resonance in order to do so [31] [32]
- The costraint on planet masses are on the order of $5-7M_J$ as a lower limit mass. These values are required in order to have a stable orbit for the planets [31]
- The orbits are nearly circular and coplanar [31] [32]

Finally, it is discussed a possible inner planet f, which is expected to lie on the resonance ratio 3e:1f and 2e:1f : it would be detected by SPHERE-IFS with masses greater than $3-7M_J$. Following previous stability simulations, Zurlo et al (2015) estimated that for the 3e:1f orbit $2-4.5M_J$ planets are not excluded, and in the 2e:1f orbit there is a possibilty of $1.5-3M_J$ planets.

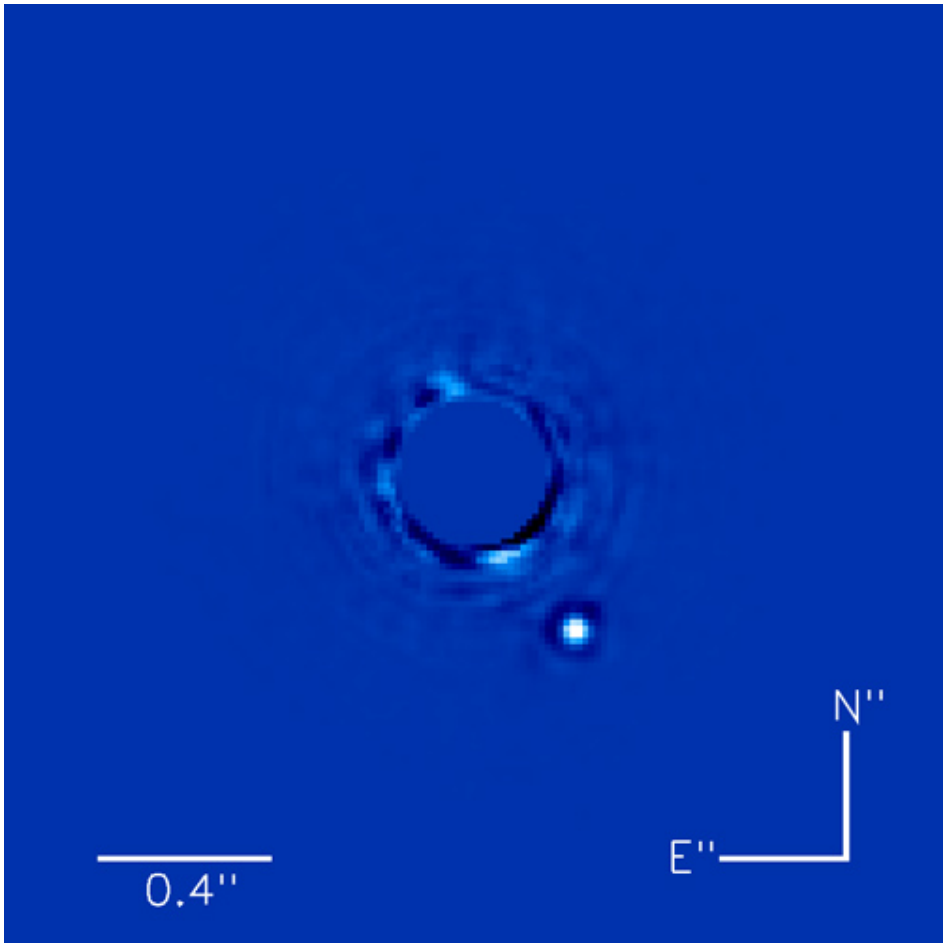

Figure 3.2: An image of β Pictoris with the High Contrast Imaging technique in which the planet is clearly visible [37]

3.1.2 β Pictoris

β Pictoris [fig:3.2] is the second brightest star in the constellation of Pictor. It is located 19.44 pc from the Solar System, and its $M_{star} = 1.83\ M_{\odot}$ and its $L_{star} = 8.7\ L_{\odot}$. The Beta Pictoris system is very young ($\sim 12\ 10^6\ yr$), although it is already in the main sequence stage of its evolution. It has a disk gap of 50 au and its spectral type A6V[38].

β Pictoris shows an excess of infrared emission compared to normal stars of its type, which is caused by large quantities of dust and gas near the star. Detailed observations reveal a large disk of dust and gas orbiting around it, which was the first debris disk to be imaged around another star. In addition to the presence of several planetesimal belts and cometary activity, there are indications that planets have formed within this disk and that the processes of planet formation may still be ongoing. Material from the Beta Pictoris debris disk is thought to be the dominant source of interstellar meteoroids in the Solar System.

β Pictoris result are very precise and is one of the first stars with directly imaged planets. This planet was imaged by Lagrange et al (2008). The instrument NACO

performed several follow ups observations, which allowed to characterize the orbit and to perform a physical characterization of it.

Moreover, there are some important results on the orbital, observational and dynamical point of view:

- The total mass of the System is $M_T = 1.83 \pm 0.04 M_{\odot}$. The contribution of the planet and the disk is low [33]
- The GPI astrometric error is extremly precise, with an error range within 1 mas [34]
- The planet mass was evaluated to be $M \sim 10 M_J$ [34]
- The orbit is nearly circular and with a semimajor axis of 10.78 au [34]

3.1.3 HD142527

HD 142527 [fig:3.3] is a binary star system in the Lupus star-forming region, at a distance of 140 pc from the Solar System [45]. It is very young, but the age is not precise: in fact, the presence of possible multiple companion can affect the age of the system. In one of the most recent age calculation, the value is ~ 5 Myr. [35]

It is notable for its protoplanetary disk and its discovery has helped refine models of planet formation. However, as it will be seen, its structure is rather complicated. The most prominent characteristic of the system are its inner and outer disk, which are separated by a 100 au distance.

In short it's a binary system, with an inner disk, an outer disk and a big gap between them: between the two there is narrow filament of gas. Also on the outer region there are gas spirals. Finally the low mass companion ($M_b \sim 0.13$ $M_{\odot}$) was found at a separation of 140 mas [35]

There are a few interesting proprieties that should give some results in the future, which are:

- There is a large amount of structure present in the outer disk. There are counted at least six spiral arms, and there are two prominent holes seen in the disk
- The gap between the (unseen) inner disk and the massive outer disk is large and mostly empty. It was detected only a faint, if any, scattering in the inner region and demonstrate the perpendicular optical depth to be at most ~ 0.01. It was also suggested that the non detection of any small-grain correspond to the gas "streamers"
- The polarization efficiency in the disk is larger in the eastern far side of the disk than in the western (near) side. This is consistent with scattering theory and previous results, although it was measured a significantly higher polarization fraction of $\sim 20 - 45\%$.

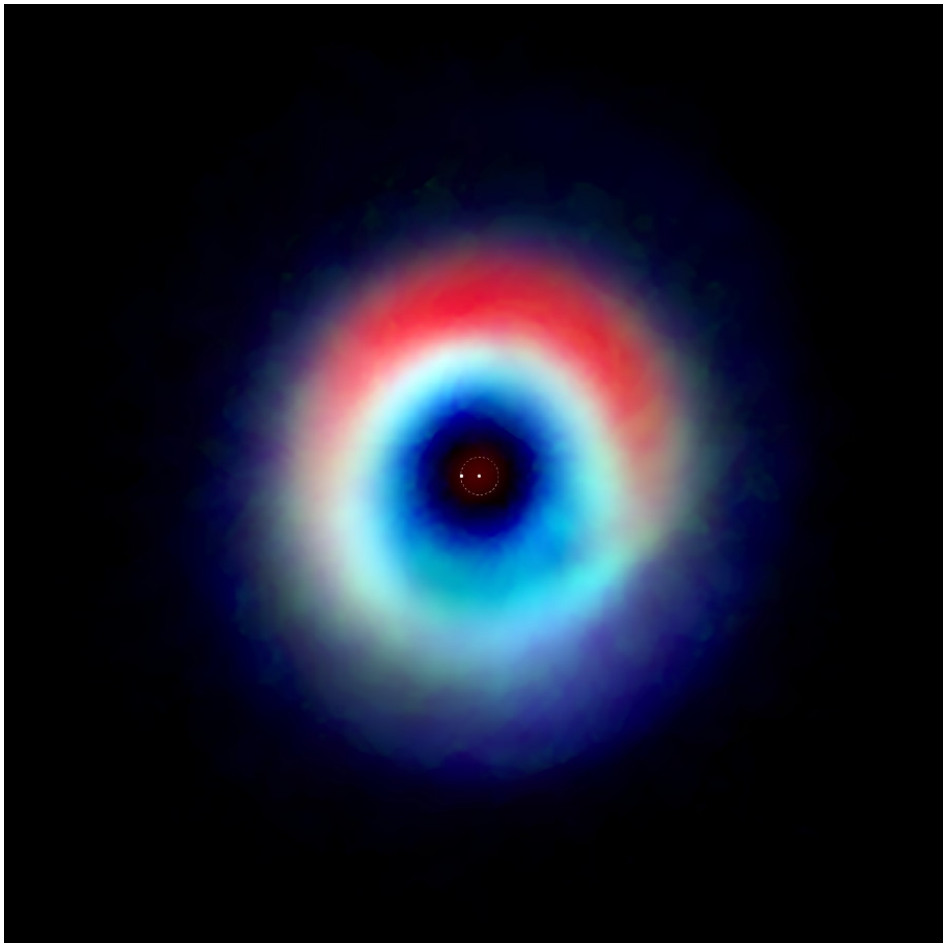

Figure 3.3: An image by ALMA, where were drawn the location of the star and its stellar companion. Credits to Andrea Isella, Rice University

- The average color of the disk is slightly red between the H and K_s band. There seem to be small, so far unexplained color differences within the disk. Especially, the disk seems to be more red in the direction of the northern and southeastern hole.
- ALMA Cycle 0 observations of HD 142527 had revealed gaseous flows inside the dust-depleted central cavity, which is an expected feature of the formation of planetary systems. Such accretion kinematics should have counterparts in other molecular tracers, and indeed the velocity centroid map in CO(3-2) also hints at non-Keplerian flows in the spirals. Moreover recent studies proves that there is a $H\alpha$ excess emission at small separation ($60 - 70$ mas), presumably due to ongoing accretion activities (Quantz S. priv. com.)

3.2 From initial condition to the required epoch (Orbital elements of a visual binary)

Most of the dynamical problems in this code are related to two-body problems. In order to work in the Thiele-Innes (TI) formalism [36], the parameters are changed in respect of the classic two-body problem. This method is used for the semplification and linearization of the orbital parameters. A graphical representation is in [fig:3.4]

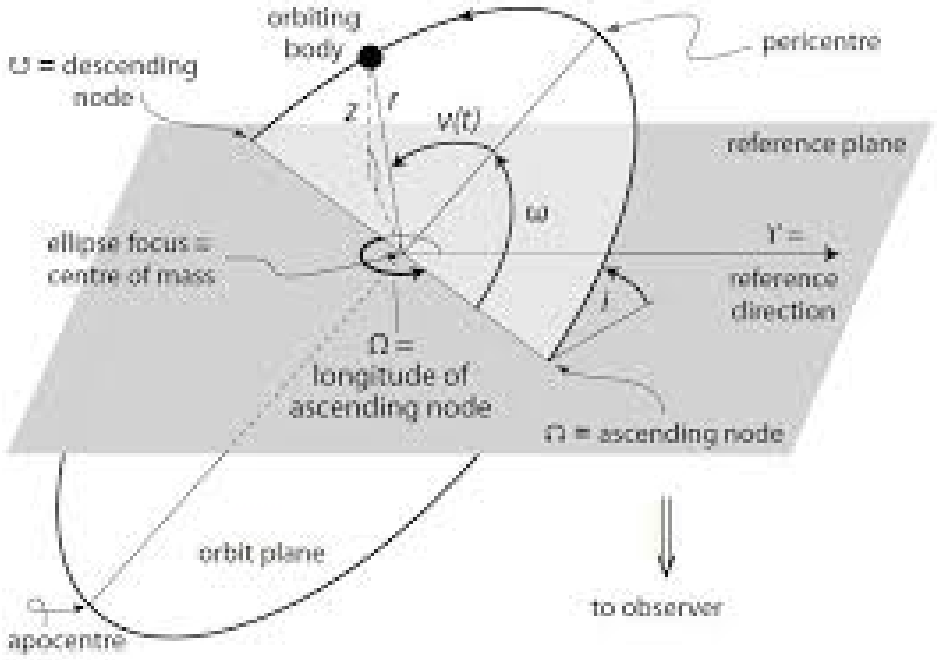

Figure 3.4: The reference plane in respect of the orbital plane [36]

It is important to remember that the apparent changes of a orbital element is caused by precession, tangential and radial motion:

- Precession motion. The precession motion shifts the North direction which is the zero line of all position angles. The correction formula is:

$$\theta - \theta_0 = \Omega - \Omega_0 = 0^\circ 00557 \sin(\alpha) \sec(\delta)(t - t_0) \tag{3.1}$$

  where θ is the position angle, α is the angle between the plane of orbit and the proper motion, δ is the angle of precession. The position angles are thus reduced to a common equinox t_0. Computing the data, the equinox is then reduced back from t_0 to the epoch t.

- Proper motion. The change in position for the proper motion is given by:

$$\theta - \theta_0 = \mu_\alpha \sin(\alpha) \sec \delta(t - t_0) \tag{3.2}$$

where μ_α is the proper motion components (both radial and tangential) in degrees. Generally, this term is neglectable. However for a binary star system, is very important. So, giving μ as the annual proper motion and Ψ the position angle, it's possible to calculate the annual changes of some orbital elements:

$$\Delta i = \mu \sin(\Psi - \Omega) \tag{3.3}$$

$$\Delta \omega = \mu \cos(\Psi - \Omega) \csc i \tag{3.4}$$

$$\Delta \Omega = \mu[\tan \delta \sin \Psi - \cot i cos(\Psi - \Omega)] \tag{3.5}$$

The radial motion affects the semi-major axis, so

$$\Delta a = -1.0227\ 10^6 a V \pi \tag{3.6}$$

where V is the radial velocity and π is the parallax in arc sec.

Now that it is known how the orbital elements changes, it is possible to introduce the Thiele-Innes formalism. It is a construction that, in respect to the orbital elements, is better suited to calculate rectangular coordinates:

$$A = a(\cos \omega \cos \Omega - \sin \omega \sin \Omega \cos i) \tag{3.7}$$

$$B = a(\cos \omega \sin \Omega + \sin \omega \cos \Omega \cos i) \tag{3.8}$$

$$F = a(-\sin \omega \cos \Omega - \cos \omega \sin \Omega \cos i) \tag{3.9}$$

$$A = a(-\sin \omega \cos \Omega + \cos \omega \cos \Omega \cos i) \tag{3.10}$$

The radial coordinate are instead represented by these two constants:

$$C = a \sin \omega \sin i \tag{3.11}$$

$$F = a \cos \omega \sin i \tag{3.12}$$

So it's possible to interact from orbital and TI elements via:

$$A + G = a(1 + \cos i) \cos(\Omega + \omega)\ B - F = a(1 + \cos i) \sin(\Omega + \omega) \tag{3.13}$$

$$A - G = a(1 - \cos i) \cos(\Omega - \omega)\ B - F = a(1 - \cos i) \sin(\Omega - \omega) \tag{3.14}$$

and the reversed equations:

$$\tan(\Omega+\omega)=\frac{B-F}{A+G}\ \ \tan(\Omega-\omega)=\frac{B+F}{A-G} \tag{3.15}$$

In the code, there is the routine thieleinnes.pro that return the coordinates of a binary at the required epoch for the assumed orbital elements.

3.3 Montecarlo method

Monte Carlo methods can be generally defined as a broad class of computational algorithms that rely on repeated random sampling to obtain numerical results. There are various method, but they tend to follow a particular pattern: define a domain of possible inputs, generate inputs randomly from a probability distribution over the domain, perform a deterministic computation on the inputs, aggregate the results.

By using probability distributions, variables can have different probabilities of different outcomes occurring. Probability distributions are a much more realistic way of describing a lot of uncertainties, especially on the unsolvable problems (like the n-body problems or multi-dimensional integrals). Common probability distributions include:

- Gaussian: The user simply defines the mean or expected value and a standard deviation to describe the variation about the mean. Values in the middle near the mean are most likely to occur. It is symmetric.
- Lognormal: Values are positively skewed, not symmetric like a normal distribution. It is used to represent values that don't go below zero but have unlimited positive potential.
- Uniform: All values have an equal chance of occurring, and the user simply defines the minimum and maximum.
- Poissonian: It expresses the probability of a given number of events occurring in a fixed interval of time and/or space if these events occur with a known average rate and independently of the time since the last event.
- Triangular: The user defines the minimum, most likely, and maximum values. Values around the most likely are more likely to occur.
- Discrete: The user defines specific values that may occur and the likelihood of each.

During a Monte Carlo simulation, values are sampled at random from the input probability distributions. Each set of samples is called an iteration, and the resulting outcome from that sample is recorded. Monte Carlo simulation does this n-times (where n depens on a lot of factors such distribution and type of result requested), and the result is a probability distribution of possible outcomes. In this way, Monte Carlo simulation provides a much more comprehensive view of what may happen.

Monte Carlo simulation provides a number of advantages over deterministic, or "single-point estimate" analysis:

- Probabilistic Results. Results show not only what could happen, but how likely each outcome is.
- Graphical Results. Because of the data a Monte Carlo simulation generates, it's easy to create graphs of different outcomes and their chances of occurrence.
- Sensitivity Analysis. With just a few cases, deterministic analysis makes it difficult to see which variables impact the outcome the most. In Monte Carlo simulation, it's easy to see which inputs had the biggest effect on bottom-line results.
- Scenario Analysis: In deterministic models, it's very difficult to model different combinations of values for different inputs to see the effects of truly different scenarios. Using Monte Carlo simulation, analysts can see exactly which inputs had which values together when certain outcomes occurred. This is invaluable for pursuing further analysis.
- Correlation of Inputs. In Monte Carlo simulation, it's possible to model interdependent relationships between input variables.

In this work, the Montecarlo method is used to explore the orbital solution: it is studied the correlation between data from astrometrical data of directly-imaged objects and the positions calculated for a broad range of potential orbital parameters and the data found by computation. In this way it's possible to define a range for the orbital fitting, reducing it even more via least square fit.

3.4 Least Square fit

A mathematical procedure for finding the best-fitting curve to a given set of points by minimizing the sum of the squares of the offsets ("the residuals") of the points from the curve. The sum of the squares of the offsets is used instead of the offset absolute values because this allows the residuals to be treated as a continuous differentiable quantity. However, because squares of the offsets are used, outlying points can have a disproportionate effect on the fit, a property which may or may not be desirable depending on the problem at hand. "Least squares" means that the overall solution minimizes the sum of the squares of the errors made in the results of every single equation.

The objective consists of adjusting the parameters of a model function to best fit a data set. A simple data set consists of n points (data pairs) (x_i, y_i) , $i = 1, ..., n$, where x_i is an independent variable and y_i is a dependent variable whose value is found by observation. The model function has the form $f(x, \beta)$, where m adjustable parameters are held in the vector β. The goal is to find the parameter values for the model which

"best" fits the data. The least squares method finds its optimum when the sum, S, of squared residuals

$$S = \sum_{i=1}^{n} {r_i}^2 \tag{3.16}$$

is a minimum. A residual is defined as the difference between the actual value of the dependent variable and the value predicted by the model. Each data point has one residual. Both the sum and the mean of the residuals are equal to zero.

$$r_i = y_i - f(x_i, \boldsymbol{\beta}). \tag{3.17}$$

A data point may consist of more than one independent variable. For example, when fitting a plane to a set of height measurements, the plane is a function of two independent variables, x and z, say. In the most general case there may be one or more independent variables and one or more dependent variables at each data point. In this case it can be defined the linear and non-linear approach:

- The linear least squares fitting technique is the simplest and most commonly applied form of linear regression and provides a solution to the problem of finding the best fitting straight line through a set of points. In fact, if the functional relationship between the two quantities being graphed is known to within additive or multiplicative constants, it is common practice to transform the data in such a way that the resulting line is a straight line, say by plotting T vs. $\sqrt{l}$ instead of T vs l in the case of analyzing the period T of a pendulum as a function of its length l. For this reason, standard forms for exponential, logarithmic, and power laws are often explicitly computed. The formulas for linear least squares fitting were independently derived by Gauss and Legendre.

- For nonlinear least squares fitting to a number of unknown parameters, linear least squares fitting may be applied iteratively to a linearized form of the function until convergence is achieved. However, it is often also possible to linearize a nonlinear function at the outset and still use linear methods for determining fit parameters without resorting to iterative procedures. This approach does commonly violate the implicit assumption that the distribution of errors is normal, but often still gives acceptable results using normal equations. Depending on the type of fit and initial parameters chosen, the nonlinear fit may have good or poor convergence properties. If uncertainties (in the most general case, error ellipses) are given for the points, points can be weighted differently in order to give the high-quality points more weight.

3.5 χ^2_{red} verification

A chi-squared test is any statistical hypothesis test in which the sampling distribution of the test statistic is a chi-square distribution when the null hypothesis is true.

Chi-squared tests are often constructed from a sum of squared errors, or through the sample variance. Test statistics that follow a chi-squared distribution arise from an assumption of independent normally distributed data, which is valid in many cases due to the central limit theorem. A chi-squared test can then be used to reject the null hypothesis that the data are independent.

Generally the final goal is to obtain a goodness of fit statistic. In the case where the variance of the measurement error is known, is to construct a weighted sum of squared errors:

$$\chi^2 = \sum \frac{(O-E)^2}{\sigma^2} \tag{3.18}$$

where σ^2 is the known variance of the observation, O is the observed data and E is the theoretical data. This definition is only useful when one has estimates for the error on the measurements, but it leads to a situation where a chi-squared distribution can be used to test goodness of fit, provided that the errors can be assumed to have a normal distribution.

The reduced chi-squared statistic is simply the chi-squared divided by the number of degrees of freedom (reduced χ^2 verification).

$$\chi^2_{\text{red}} = \frac{\chi^2}{\nu} = \frac{1}{\nu}\sum \frac{(O-E)^2}{\sigma^2} \tag{3.19}$$

where ν is the number of degrees of freedom, likely given by $\nu = N - n$, where N is the number of observations, and n is the number of fitted parameters. The advantage of the reduced chi-squared is that it already normalizes for the number of data points and model complexity. This is also known as the mean square weighted deviation.

As a rule of thumb (again valid only when the variance of the measurement error is known a priori rather than estimated from the data), a $\chi^2_{\text{red}} \gg 1$ indicates a poor model fit. A $\chi^2_{\text{red}} > 1$ indicates that the fit has not fully captured the data (or that the error variance has been underestimated). In principle, a value of $\chi^2_{\text{red}} = 1$ indicates that the extent of the match between observations and estimates is in accord with the error variance. A $\chi^2_{\text{red}} < 1$ indicates that the model is 'over-fitting' the data: either the model is improperly fitting noise, or the error variance has been overestimated. Due to the semplification of the code, a $\chi^2_{red} \leq 2$ will be considered a good data limit.

3.6 Code description

The code uses the Monte Carlo method, as previously discussed. In this section, it will be given a step by step work of it, while the physical meaning will be explained later.

1. Set the number of iterations for the general code. This repetition is strictly used for the Monte Carlo method.

2. Organize the data. The astrometric data file is taken and then re-organized.

3. Put the literature data and transform them into the Thiele-Innes formalism.

4. Orbital fitting between the astrometrical (orbit) and literature data (points).

5. χ^2_{red} test: if the test is good enough the data can be used as a data reference for the Monte Carlo simulation.

6. Start of the MC simulation part of the code. It's entered a number of iteration of the Monte Carlo simulation and the same simulation is repeated from the number of iterations from point 1: the MC iteration will give diffent set of data, while a different set of MC simulation data for every code iteration will give different possible result. This procedure is done to assure a lot of variance in the simulation and so a lot of possible data.

7. Select a range of values for the orbital parameters where the simulations should find the diffent parameters values. These numbers could be build on the previous results from the literature to save computing time, If orbital elements are not avaible, a broad exploration of the parameter space (great range of values of the individual parameter) needs to be performed, in order to avoid missing possible solutions.

8. Again there is the conversion of data into the Thiele-Innes formalism, and then the mean value and standard deviation of the orbital parameters are computed.

9. The χ^2_{red} is computed.

10. 8 and 9 point are computed for every iteration of the MC simulation.

11. The values are filtered by a limit value applied to the χ^2_{red}: in all the cases this number is 2.0.

12. The data is ready.

There are three fundamental points to follow in order to work with the program:

- Kepler approximation: the semi-major axis is evaluated via Kepler third law. In this istance the most precise solutions are found when the first body is a lot greater than the second one and, in the presence of multiple bodies like the solar system, the planets are indipendent from each other. This is true both for HR8799 and Beta Pic. For HD 142527, because the first and second body are comparable in mass, the sum of masses is included in the 3rd Kepler law.

- Negligence of some gravitational and non forces: There are possible elements that can harden the system situation. In HR8799 there is the planet-planet perturarbation, and the fact that the planets are not indipendent from the star (they are in resonance with it). However via prior studies, there were analyzed different resonance stability ratios between planets, and so the orbital elements are declared "indipendent" for that reason. Moreover the planet-planet perturbation

are neglected. In the other two system there are not particular approssimations. As the observational time baseline is shorter than the orbital period, phenomena acting on long timescales as planet migration or the tidal interaction of the star, can be safely neglected.

- Disk presence: the presence of the disk is fundamental in order to shorten the number of possible orbits. The different shape from stellar system to stellar system give different possible orbits.

3.7 Application

In order to let the code work, it was necessary to use readfile.pro, a auxiliary function to read a text file with known number of columns and unknown number of rows. Moreover there was the Thieleinnes.pro file, which used the Thiele-Innes set of coordinates in order to work with the orbital parameters in a square representation (as seen before).

HR8799 and β Pictoris have a precise set of orbital elements data in the literature, while HD142527 is not completed. The astrometric data were precise for all the systems. For this reason, the last stellar system were not started as an evaluation of the system literature data, but as an experiment, in order to find different set of datas with the newest data from SPHERE. It was assumed the same as HD 142527 for β Pictoris, as a test to experiment the data with a full defined orbit. In the previous section it was explained the code description in general, here it's done in the specific physics assumptions made for the star system. In order to understand that, there are four steps:

- The dataset verification: In order to verify the best set of data for the MC simulation, the astrometric data and the literature data are verified. This step is necessary to find a good set of values for the next step. This verification is done with the χ^2_{red} test: if the residuals fits the data then the literature dataset is good. In this program the verification is done by orbital parameters, which are from the literature, and the position (in this case are used declination and right ascension) of the star in the sky. The data fit is confirmed by the verification of the position change in time.

  The final result was also tested, via χ^2_{red} verification, which confirmed the first assumption in all cases.

- The dataset for the Monte Carlo simulation: the second part is to understand the dataset for the MC simulation. In this istance it's important to have in mind that a greater interval range is a compromise between a pro and a con: the pro is that the good data range is better defined, the con is that there is a greater computational time. All the data that are formed from a generation of numbers, are data which can be completly false or true. Again a confirmation is used by the χ^2_{red} verification. The best value for a χ^2_{red} method is 2, which was applied in all cases.

The correct procedure to find a great set of data is:

1. Do some exploration with a χ^2_{red} limit greater than the one you take for data
2. Reduce the interval range in order to obtain major good data in a cheaper computational time, with a proper χ^2_{red} limit

- Reapeat the code: Good datas were found from 1000 iterations, best datas from 5000 iterations and finally a large set of good data, 10000, is used fo the parameters correlation, in order to have a great amount of data and the best values. In general, the required number of iteration depend on the amount and/or quality of the data, the orbital coverage of the orbit, the required accuracy (as an example, the Monte Carlo method gives an estimate value, not a precise one) and finally the computer power.

- Final results: the final result is the verification of the best orbital parameters that describes the star system and to find the correlation between them. In the first case there is an interval assumption of the best value of the orbital parameters, while in the second one if there is a connection between data. This final point is the most important one, which will be explained in detail for every star system.

Chapter 4

Scientific Results and theoretical confrontation

The final result and the procedure used for the systems is illustrated here. In this part of the work the application of the code, presented in the previous chapter, is shown the orbital parameters symbols are: a for the semi-major axis, p for period, i for inclination, e for eccentricity, Ω for the longitude of the ascending node, ω for the argument of the periastron, T_0 for the passage at the periastron.

4.1 HR8799

The HR8799 system was chosen because the code was originally designed for this system. In particular additional data are avaible with respect to the previous application (Zurlo et al 2015 versus Esposito et al 2013) and so it is used again to verify the goodness of data. HR8799 has 4 planets and, when running the code, we made the assumption that every planet of this system is indipendent from each other. The astrometrical data are in [tab:4.1]

The literature dataset was given by Zurlo et al (2015): these data are from a SPHERE's spectrophotometrical and astrometrical method. The fit with the astrometrical data had a $\chi^2_{red,b} = 1.38$, $\chi^2_{red,c} = 1.59$, $\chi^2_{red,d} = 1.84$ and $\chi^2_{red,e} = 4.39$ (this one is greater than the others because it has less defined data).

Appropiate coordinate transformation was performed in order to ensure the data and the calculated values are in the same quadrant.

The data set of Zurlo and Esposito are in [tab:4.2]

The starting point is the application of the χ^2_{red} test in order to analyze the goodness of Zurlo's datas. The process consist specifically in the use of the orbital parameters transformation in the Thiele-Innes formalism. After that there is a plot of the literature data (points) against the astrometric data (the line). If the fit is good, then it's possible to go in the next phase. In the first set of images, there is the orbital fit [fig:4.1][fig:4.2], while in the second set of images [fig: 4.3][fig: 4.4], there is the residual with respect to the orbital solution plotted before.

The data of Zurlo are good, so we can use them as a starting point for the Monte

t	x_b	y_b	x_c	y_c	x_d	y_d	x_e	y_e
1998.83	1.411	0.986						
1998.83	1.418	1.004	-0.837	0.483	0.133	-0.533		
2002.54	1.481	0.919						
2004.53	1.471	0.884	-0.739	0.612				
2007.58	1.522	0.815	-0.672	0.674	-0.170	-0.589		
2007.81	1.512	0.805	-0.674	0.681				
2008.52	1.527	0.799	-0.658	0.701	-0.208	-0.582		
2008.61	1.527	0.801	-0.657	0.706	-0.216	-0.582		
2008.71	1.528	0.798	-0.657	0.706	-0.216	-0.582		
2008.89	1.532	0.796	-0.654	0.700	-0.217	-0.608		
2009.58							-0.299	-0.217
2009.58							-0.303	-0.209
2009.62	1.536	0.785						
2009.70	1.538	0.777	-0.634	0.697				
2009.76	1.535	0.816	-0.636	0.692	-0.270	-0.600		
2009.77	1.532	0.783	-0.627	0.716	-0.241	-0.586	-0.306	-0.217
2009.83	1.540	0.800	-0.630	0.720	-0.240	-0.580		
2009.83							-0.304	-0.196
2010.53							-0.325	-0.173
2010.55							-0.324	-0.175
2010.83							-0.334	-0.162
2011.79	1.579	0.734	-0.561	0.752	-0.299	-0.563	-0.326	-0.119
2011.86	1.546	0.725	-0.578	0.767	-0.320	-0.549	-0.382	-0.127
2014.53	1.570	0.707	-0.522	0.791	-0.390	-0.530	-0.386	-0.008
2014.62					-0.391	-0.529	-0.384	-0.005
2014.93	1.574	0.703	-0.518	0.797	-0.402	-0.523	-0.384	0.014

Table 4.1: Astrometric Data for HR8799 planets: the data are expressed in *arcsec* and the void data means that there wasn't an observation for the planet at the corresponding epoch. The oldest data (until 2011) are from Esposito et al 2013, while the newest are from Zurlo et al 2015.

Parameters	***Zurlo et al 2015***	***Esposito et al 2013***
Planet b		
a(au)	67.96	68.08
P(yr)	455.88	449.70
i(°)	30.27	28.00
Ω(°)	60.89	35.50
e	0	0
ω(°)	0	0
$T_0(yr)$	2006.5	1997.55
Planet c		
a(au)	42.81	42.80
P(yr)	227.94	224.9
i(°)	29.43	28.00
Ω(°)	65.68	35.50
e	0	0
ω(°)	0	0
$T_0(yr)$	1848.18	1844.10
Planet d		
a(au)	26.97	27.01
P(yr)	113.97	112.40
i(°)	38.63	28.00
Ω(°)	56.09	35.50
e	0	0.1
ω(°)	0	80.20
$T_0(yr)$	1965.27	1992.31
Planet e		
a(au)	16.99	14.66
P(yr)	56.99	44.96
i(°)	30.95	28.00
Ω(°)	145.73	35.50
e	0	0
ω(°)	0	0
$T_0(yr)$	1995.61	1987.08

Table 4.2: Literature data confrontation between the older and the newest data for HR8799 planets.

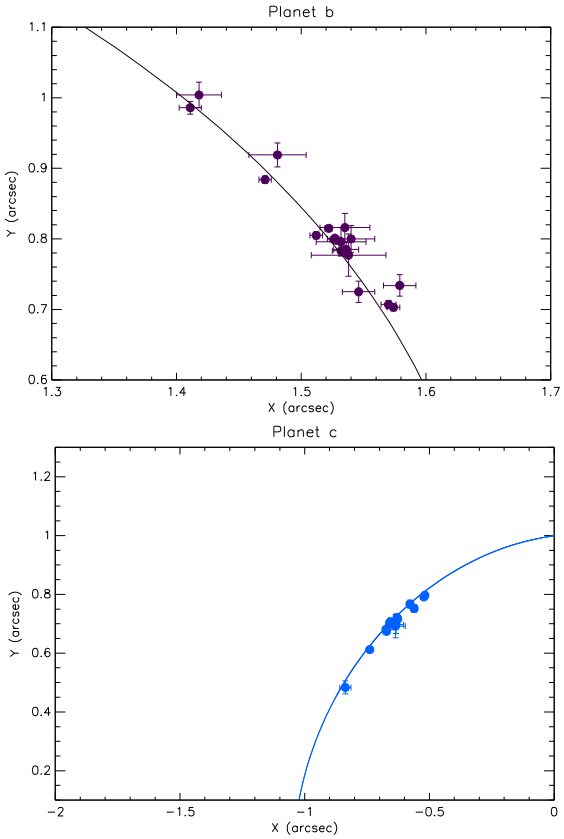

Figure 4.1: Relative astrometry of HR8799 planets b and c available in literature.The solid lines show the adopted orbital solution

Carlo simulation. Within the final data, the value of the minimum, acceptable, χ^2_{red} was 2, where the mean χ^2_{red} results where: $\chi^2_{red,b} = 1.713 \pm 0.210$, $\chi^2_{red,c} = 1.675 \pm 0.247$, $\chi^2_{red,d} = 1.639 \pm 0.278$ and $\chi^2_{red,e} = 1.713 \pm 0.210$. The mean orbital elements results are in [tab:4.3]; the error bars are given by the Gaussian standard deviation.

When running the Monte Carlo simulation over an extended grid of orbital parameters, the plot of χ^2_{red} allows to check how well the parameter is costrained by the data[fig:4.5] [fig:4.6] [fig:4.7] [fig:4.8]:

From the data, it's possible to see the correlations between the parameters [fig:4.9] [fig:4.10] [fig:4.11] [fig:4.12]

The new data are consistent with those of previous works. If we adopt the Soummer et al. (2011) orbital solution, planet e cannot be in a circular and coplanar orbit with a 2:1 mean motion resonance with d. Instead, a 5:2 resonance represents a satisfactory fit to the data, when assuming circular orbit and coplanarity with the other planets [31]. This orbital solution represents only one of the possible ones fitting the observational data. Unique determination of orbital parameters is not yet possible as the observations cover only a minor fraction of the orbital periods.

When forcing all consecutive planets to be involved in 2:1 resonances (8:4:2:1 resonance involving all the known planets), there are newfound orbital solutions that nicely

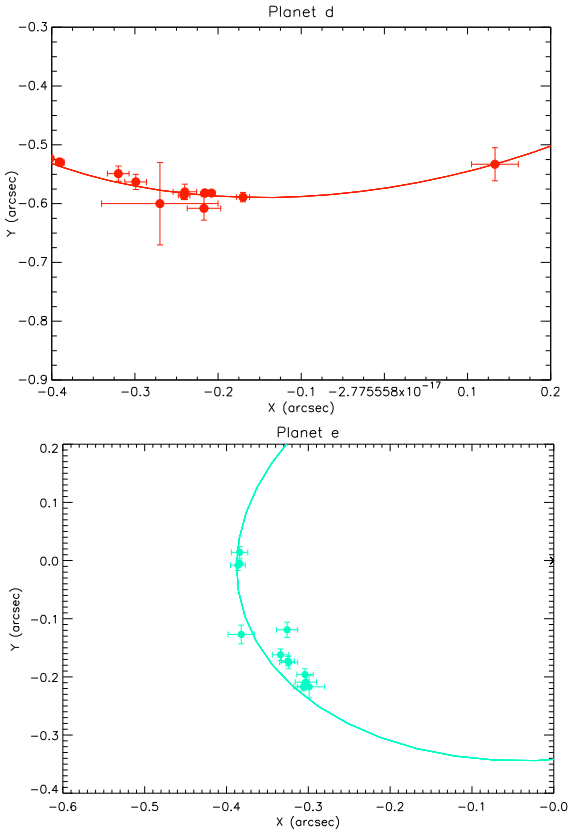

Figure 4.2: Relative astrometry of HR8799 planets d and e available in literature.The solid lines show the adopted orbital solution

Parameters	***Mean values***
Planet b	
a(au)	70.05 ± 3.15
P(yr)	469.74 ± 31.87
i$(^\circ)$	155.00 ± 14.44
$\Omega(^\circ)$	-6.30 ± 13.07
e	0.09 ± 0.07
$\omega(^\circ)$	78.95 ± 42.18
$T_0(yr)$	2147.61 ± 60.66
Planet c	
a(au)	43.93 ± 2.92
P(yr)	233.45 ± 23.40
i$(^\circ)$	145.88 ± 7.97
$\Omega(^\circ)$	39.52 ± 22.64
e	0.104 ± 0.076
$\omega(^\circ)$	110.32 ± 115.72
$T_0(yr)$	1847.64 ± 27.76
Planet d	
a(au)	28.49 ± 3.39
P(yr)	122.32 ± 21.84
i$(^\circ)$	139.46 ± 6.36
$\Omega(^\circ)$	23.75 ± 23.01
e	0.119 ± 0.078
$\omega(^\circ)$	204.83 ± 106.04
$T_0(yr)$	2069.00 ± 74.58
Planet e	
a(au)	14.74 ± 1.46
P(yr)	45.44 ± 6.81
i$(^\circ)$	159.56 ± 11.61
$\Omega(^\circ)$	19.30 ± 24.82
e	0.117 ± 0.08
$\omega(^\circ)$	149.453 ± 110.40
$T_0(yr)$	1971.23 ± 17.64

Table 4.3: Mean values of the orbital elements of the 4 HR8799 planets. The data are in perfect accord with Zurlo et al

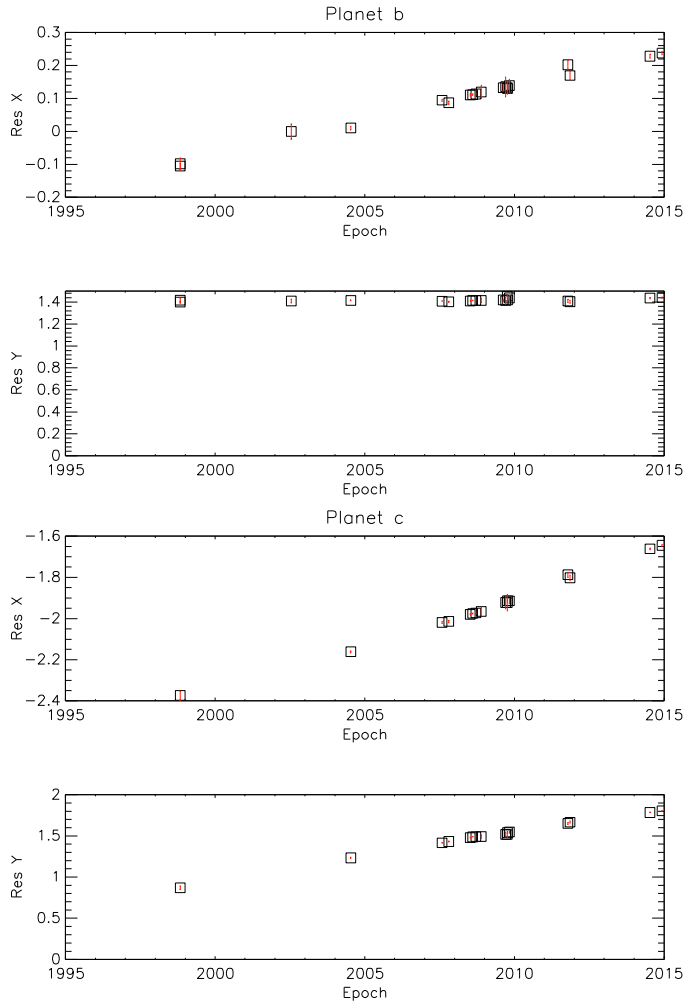

Figure 4.3: Residuals in x and y coordinates vs. time for each of the planets with respect to the orbital solution plotted before for planet b and c

fit the available data [32].

After these explorations based only on observational data, there are additional clues that can be derived from the dynamical stability of the system. Previous dynamical studies considering the three largest planets of the system (without planet e), found that only a minor fraction of the orbital solutions compatible with the astrometric observations are dynamically stable. Stability is favoured by the occurrence of a 2:1 mean motion orbital resonance between each couple of consecutive planets, low eccentricity of their orbits and by planetary masses at the low end of the plausible values derived from their luminosity and stellar age.

Sudol & Haghighipour (2012) presented a study of the dynamical stability of the 4 - planet system. They found that the system is strongly unstable with a few solutions that barely survive for ages comparable to the age of the system. Planet e is marginally fit by these stable solutions, and they proposed that HR8799e astrometry is systematically biased toward larger separations.

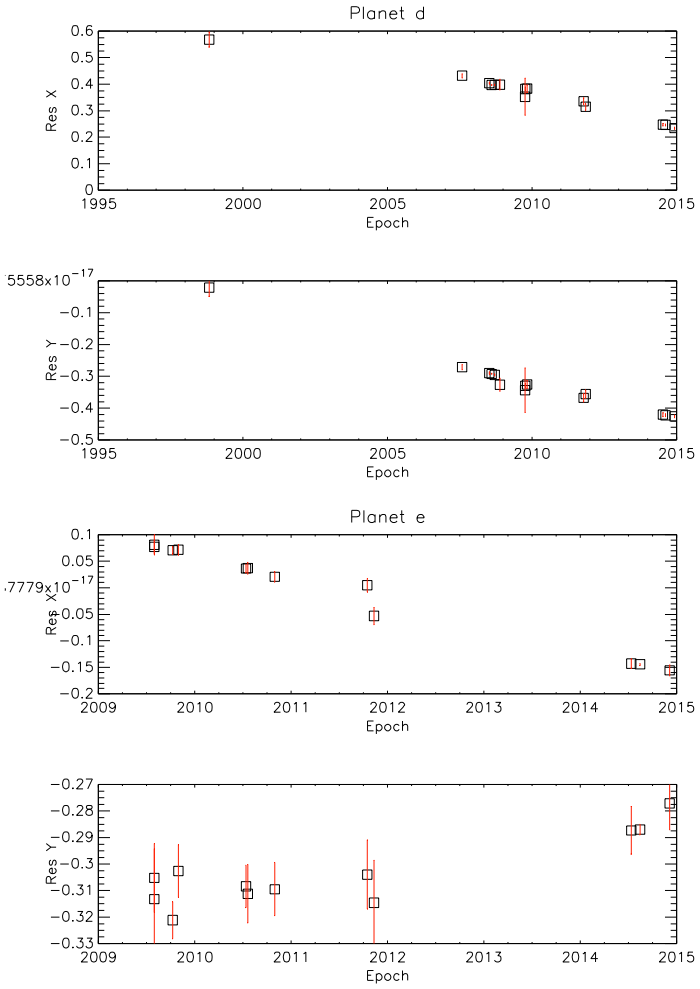

Figure 4.4: Residuals in x and y coordinates vs. time for each of the planets with respect to the orbital solution plotted before

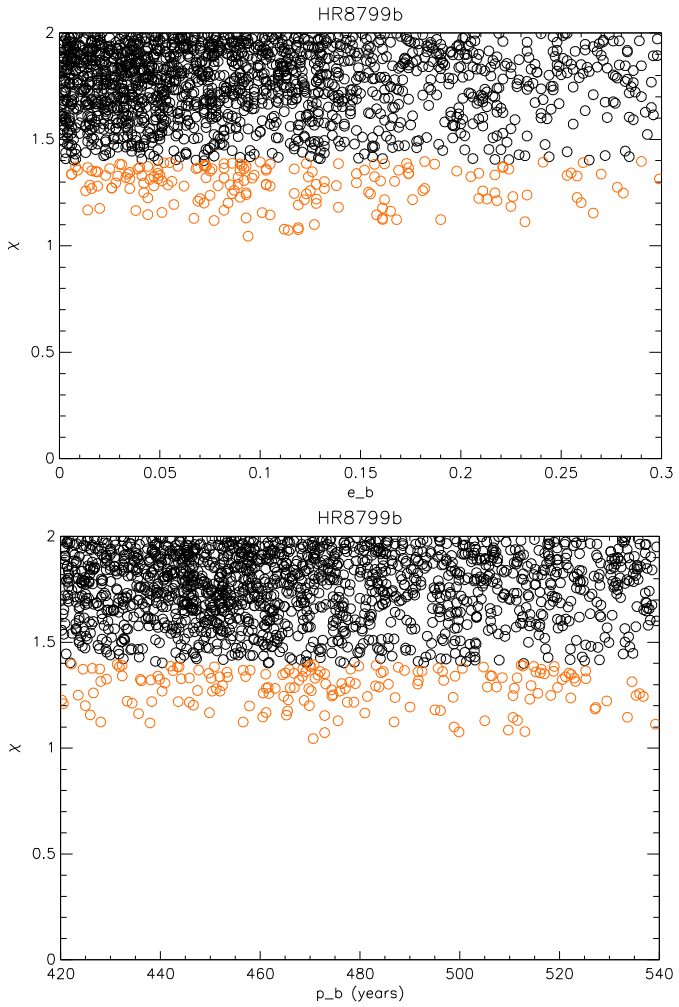

Figure 4.5: χ^2_{red} range of probable data for planet b.

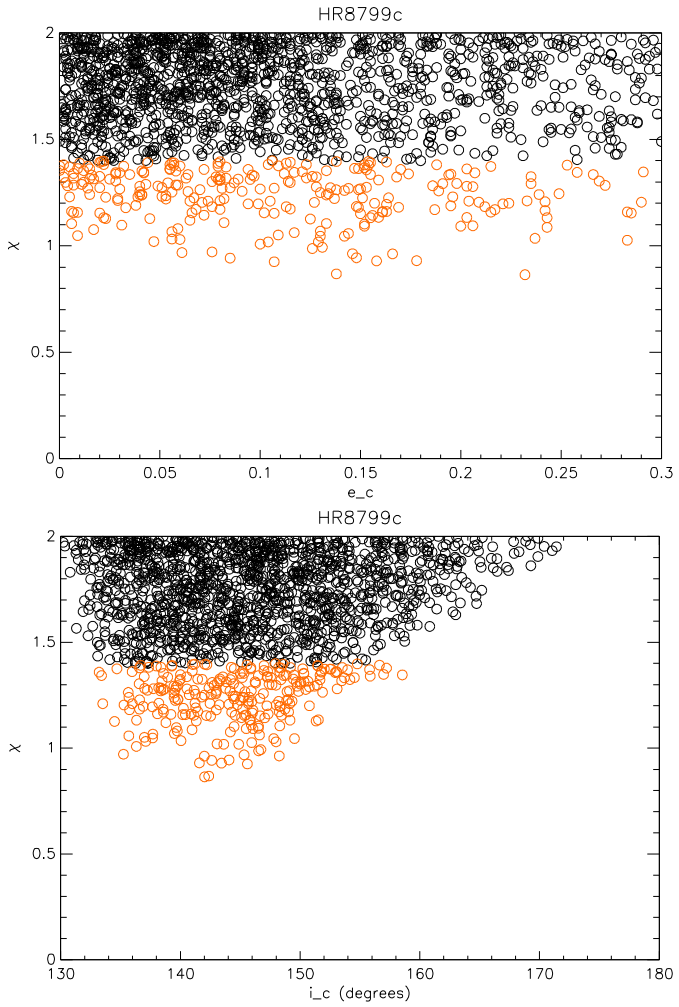

Figure 4.6: χ^2_{red} range of probable data for planet c.

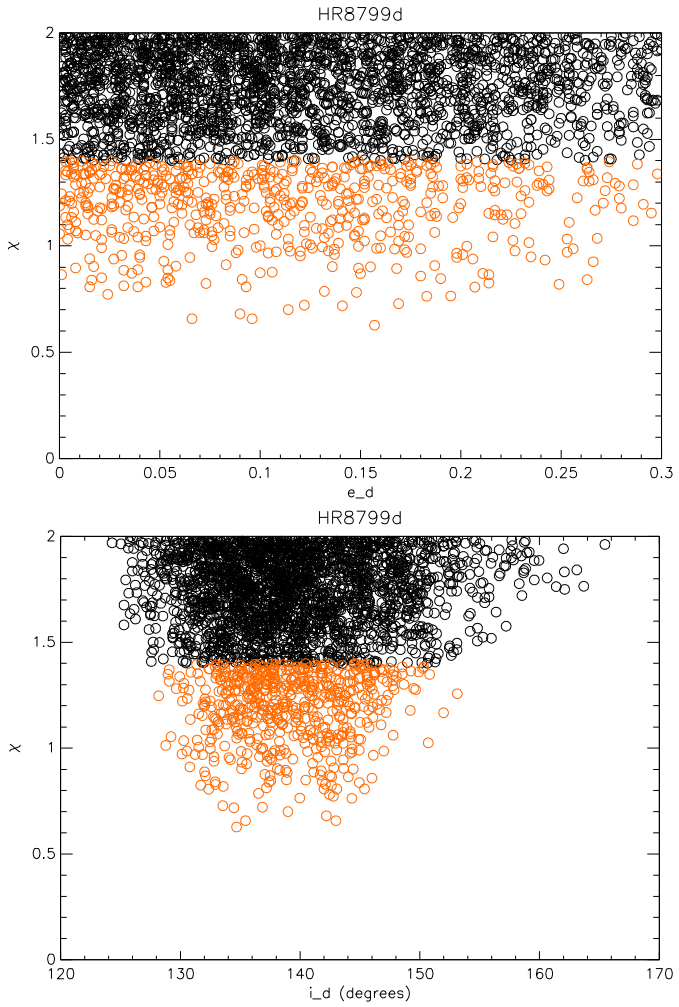

Figure 4.7: χ^2_{red} range of probable data for planet d

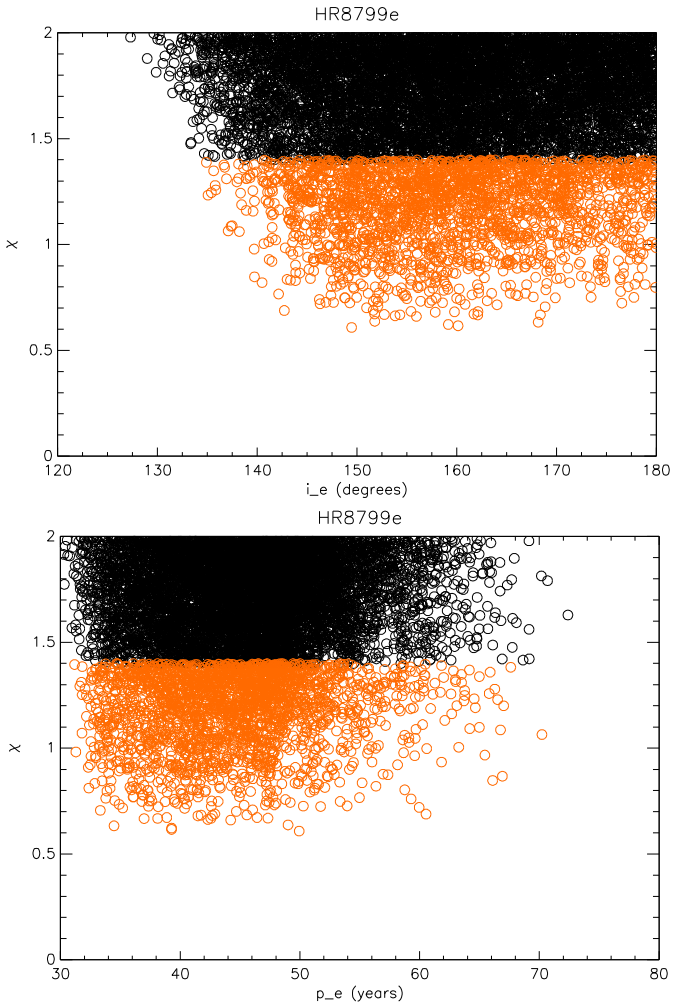

Figure 4.8: χ^2_{red} range of probable data for planet e

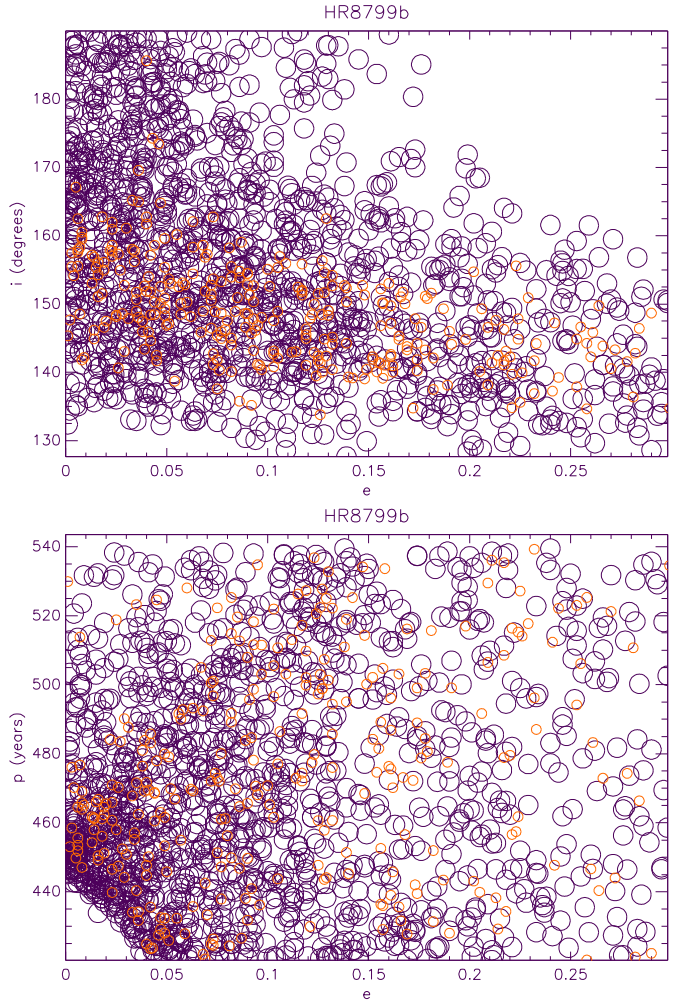

Figure 4.9: Orbital parameter correlation for planet b

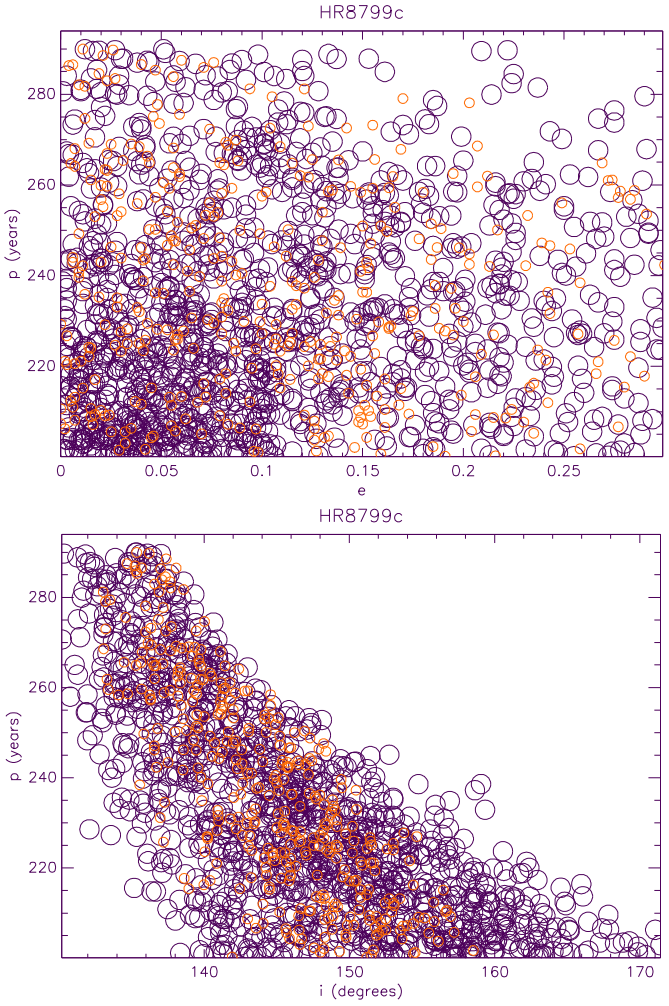

Figure 4.10: Orbital parameter correlation for planet c

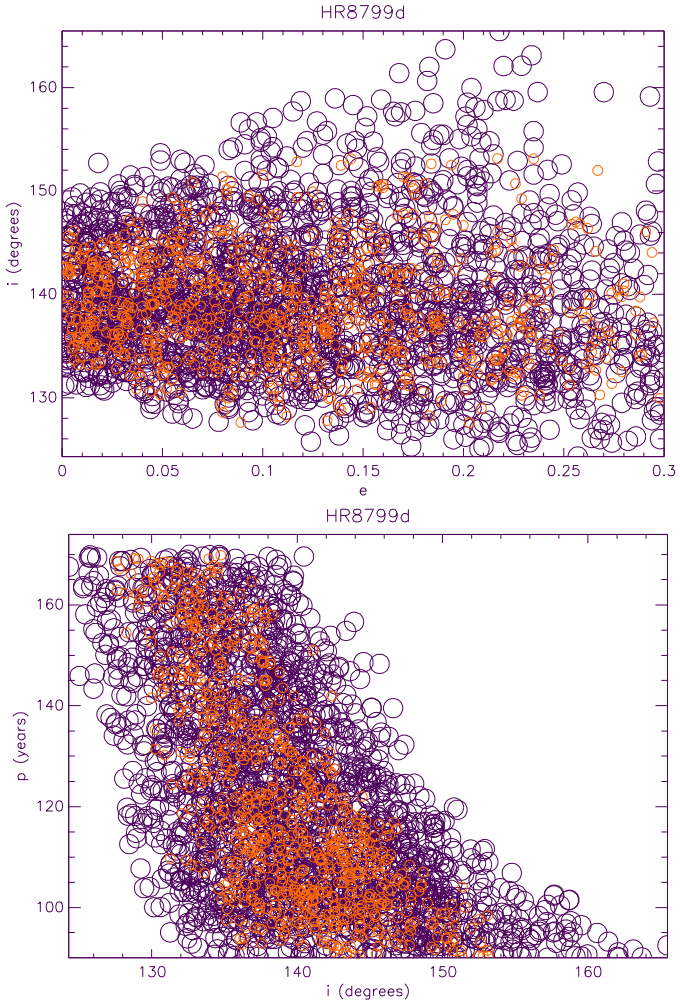

Figure 4.11: Orbital parameter correlation for planet d

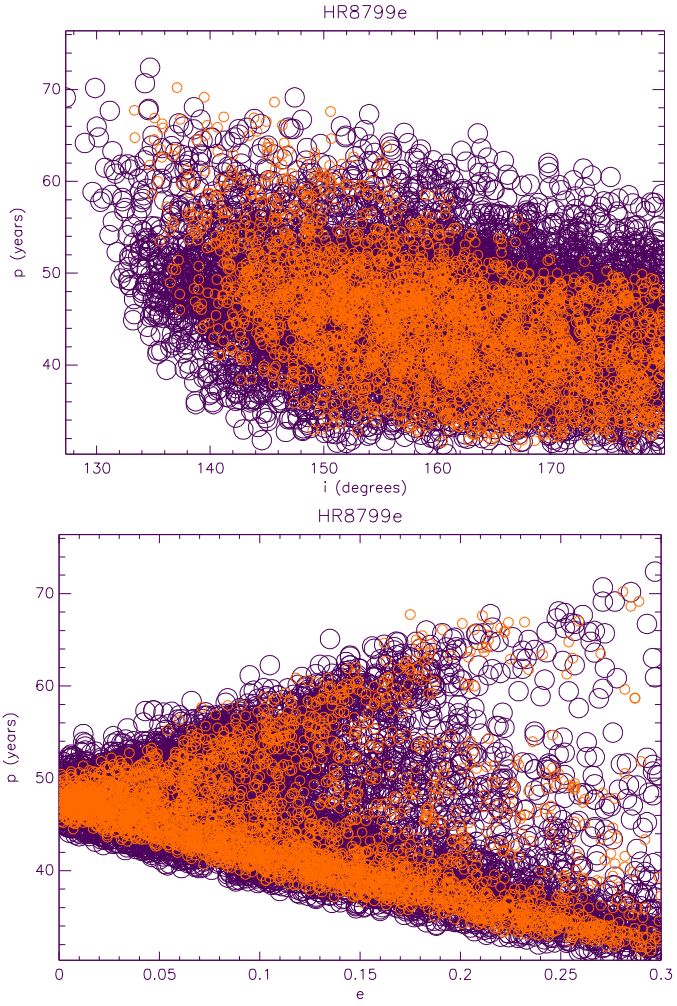

Figure 4.12: Orbital parameter correlation for planet e

Assuming stellar mass of 1.56 $M_{\odot}$[18] and the last extimated planetary masses ($M_b = 7M_J$, $M_c = 10M_J$, $M_d = 10M_J$, $M_e = 9M_J$) and finally by numerically integrating the orbits, there are highly chaotic solutions that survive on orbits similar to the observed ones for a few Myrs only. This is not compatible with the stellar age even assuming that the primordial gas disk damped the eccentricities of the planets granting stability. The disk lifetime can be no longer than $\tau \sim 20\ 10^6\ yr$. This is a conservative assumption as, according to observations, the presence of gas in the inner regions of the disk is observed only for timescales shorter than 10^7.

Two orbital solutions are favored with similar χ^2_{red}, with the orbital period ratios 2d:1e and 3d:1e in Zurlo et al. The IFS data point for planet e is out of the orbital solution with the orbital period ratio 5d:2e.

4.2 β Pictoris

β Pictoris is the simpliest star system case, but also the one with the most accurate data. Indeed the usual orbit fitting techniques can be applied to this system. It was chosen to explore the behaviour of the Monte Carlo simulations in case of well-defined parameters (good orbit coverage). The astrometric data are in [tab:4.4]

t	x_b	y_b
2003.86	0.233	0.341
2009.81	-0.153	-0.257
2009.99	-0.163	-0.260
2010.27	-0.173	-0.300
2010.74	-0.193	-0.311
2010.87	-0.207	-0.326
2010.88	-0.209	-0.330
2011.08	-0.211	-0.350
2011.23	-0.214	-0.367
2013.87	-0.229	-0.364
2013.88	-0.229	-0.365
2013.94	-0.228	-0.360
2013.94	-0.228	-0.359
2014.85	-0.194	-0.299
2015.25	-0.172	-0.266
2015.85	-0.138	-0.207
2015.93	-0.134	-0.200
2015.97	-0.130	-0.195
2016.06	-0.126	-0.186

Table 4.4: Astrometric Data for β Pictoris planet: the data are expressed in *arcsec*

In that istance the data found with the Montecarlo method are in [tab:4.5], with a mean $\chi^2_{red} = 1.676 \pm 0.270$:

The χ^2_{red} representative image can be seen in [fig: 4.13].

Parameters	*Mean values*
Planet b	
a(au)	9.36 ± 1.31
P(yr)	21.34 ± 4.60
i$(^\circ)$	87.99 ± 1.41
$\Omega(^\circ)$	-31.53 ± 90.00
e	0.18 ± 0.12
$\omega(^\circ)$	184.31 ± 101.03
$T_0(yr)$	2011.31 ± 5.44

Table 4.5: Mean values of the β Pictoris planet. The data are in perfect agreement with Wang et al (2016).

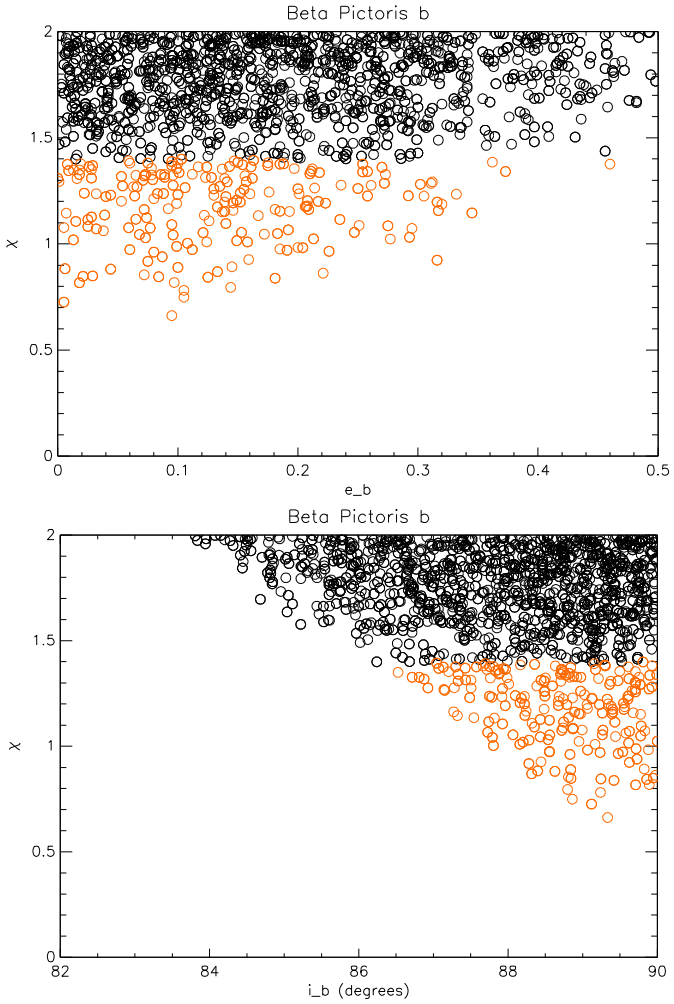

Figure 4.13: χ^2_{red} range of probable data for β Pictoris b.

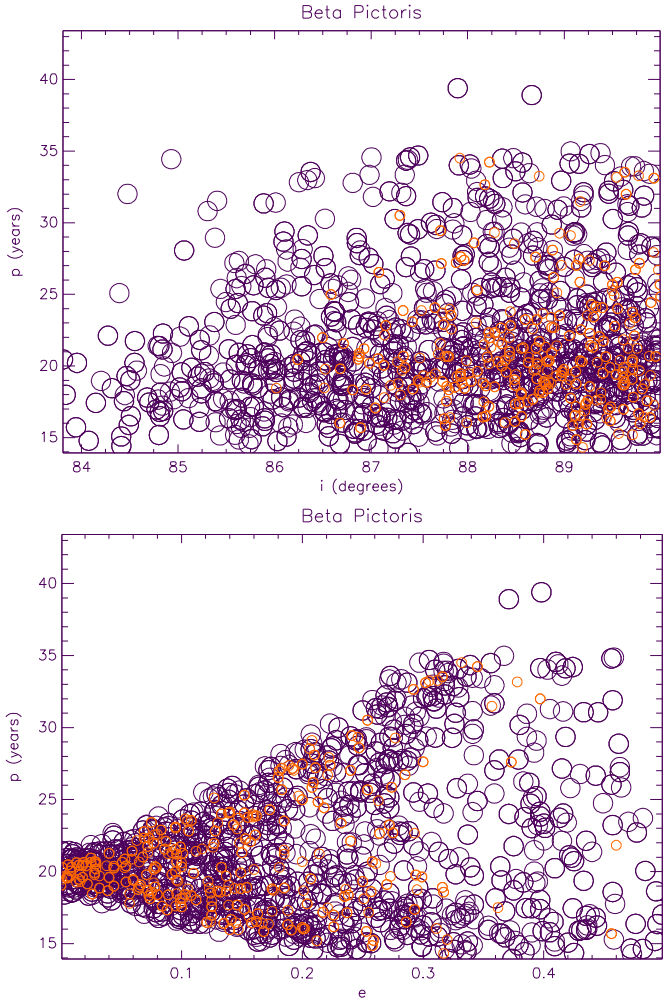

Figure 4.14: Orbital parameter correlation for β Pictoris b

The parameter correlation are following in [fig:4.14]:

From the images, the data are strictly bound to few solutions, thanks to the orbital astrometric data. The dataset is in agreement with Wang et al (2016). The behaviour of the code with this extremly precise data is good. This is a further confirmation of the goodness of the code.

4.3 HD142527

HD142527 is the main topic of this work. The problem is that the set of data (and orbital coverage) is incomplete, and the same ones where of limited accuracy due to the large contrast at $70 - 100$ mas separation (in $H\alpha$ was of $\Delta_{mag} = 7.5$ mag). The astrometric data are given by Lacour et al (2016) and SPHERE-GTO data (biased on preliminary astrometric calibration and currently being improved) data in [tab:4.6].

The problem that is adressed here is the following: is the gap between the internal

t	x_b	y_b
2012.19	0.065	-0.061
2013.20	0.066	-0.049
2013.27	0.069	-0.051
2013.45	0.069	-0.046
2014.27	0.069	-0.039
2014.31	0.074	-0.048
2014.36	0.069	-0.035
2015.37	0.070	-0.022
2016.23	0.067	-0.008
2016.45	0.063	-0.007

Table 4.6: Astrometric Data for HD142527 companion: the data are expressed in *arcsec*. The 2015 and 2016 data are the SPHERE-GTO data, while the others were taken from Lacour et al (2016).

Parameters	***Mean values***
Companion	
a(au)	18.27 ± 1.74
P(yr)	48.86 ± 6.66
i($^\circ$)	54.66 ± 3.32
$\Omega(^\circ)$	4.75 ± 5.84
e	0.62 ± 0.08
$\omega(^\circ)$	64.62 ± 7.76
$T_0(yr)$	1970.52 ± 6.81

Table 4.7: Mean values of HD 142527b

and external disk the fault of the gravitation influence of the central binary system (and so the companion is responsible for the gap) or is there room for an additional object (a planet)?

So the procedure to solve this problem starts with the MC simulation. The found orbital parameters of the binary are not unusual and well within the observed typical distribution [32]. They have a $\chi^2_{red} = 1.661 \pm 0.273$, and the mean values are in [tab:4.7]

The χ^2_{red} representative images are found in [fig:4.15][fig:4.16]

The parameter correlation are following in [fig:4.17][fig:4.18]:

From this data there is an hint of a possible high eccentricity and a moderatly short period. These 2 elements are important for the possible physical outcomes.

In order to understand if the star companion can be the responsible for the gap, it is essential to introduce the critical semi-major axis (a_c)[41]. The results of the semi-major axis are compared to my results. In order to explain what the last one is, it's important, firstly, to know the basis of its definition. In fact the value of this a_c is restricted to the binary systems, where the value should not be near the outside region (near the lagrangian points L_4 or L_5) because in that position the object would give a linear stable orbit for mass ratio less than $\mu \sim 0.04$ for motion about these points.

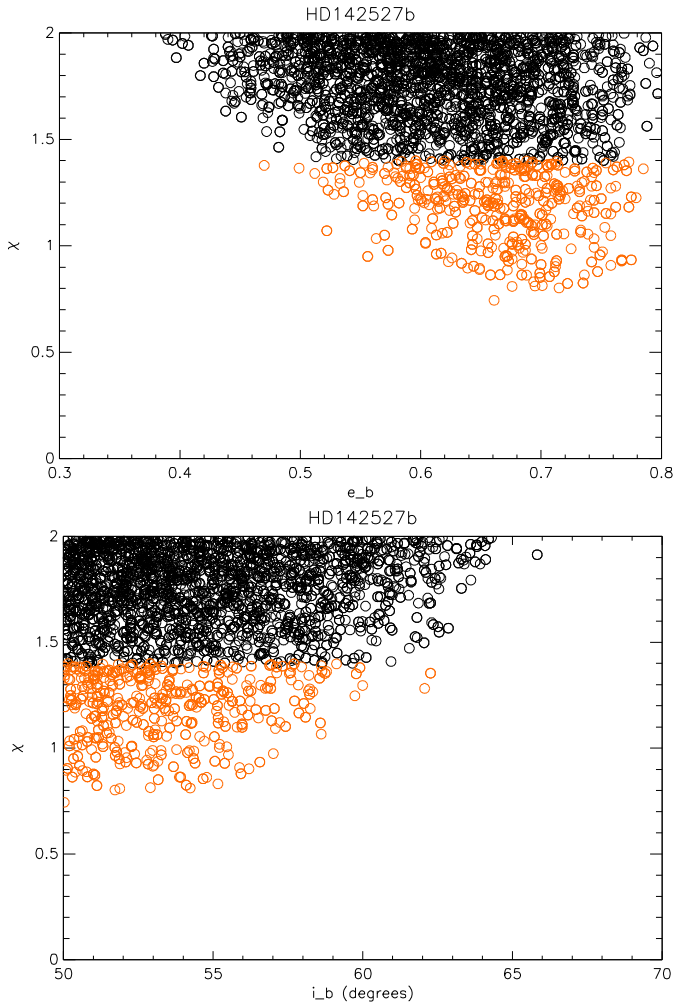

Figure 4.15: χ^2_{red} range of probable data for HD142527b.

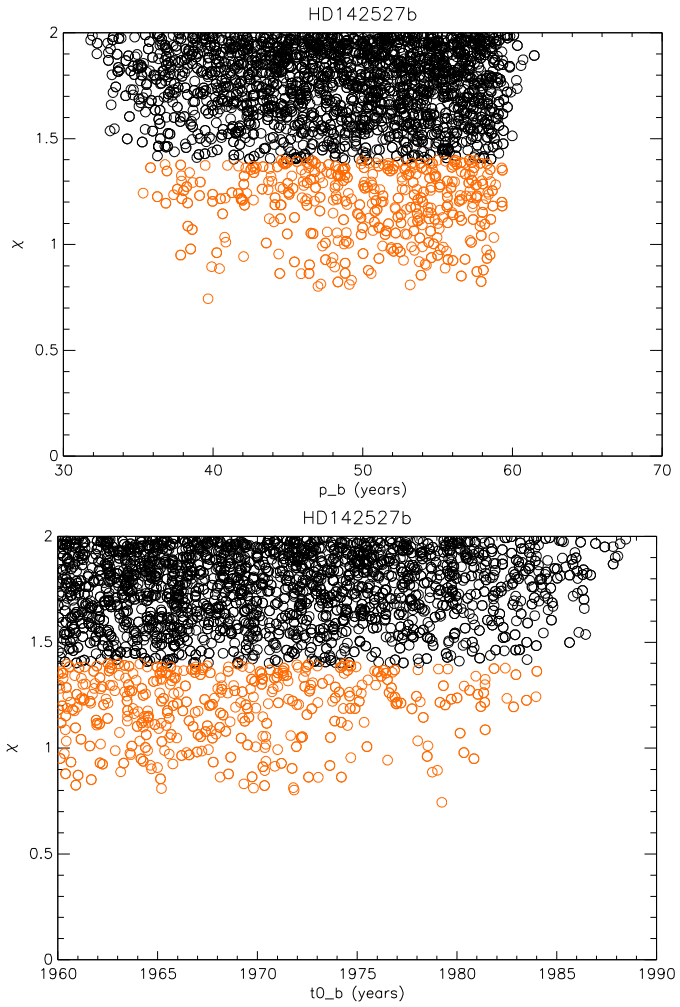

Figure 4.16: χ^2_{red} range of probable data for HD142527b.

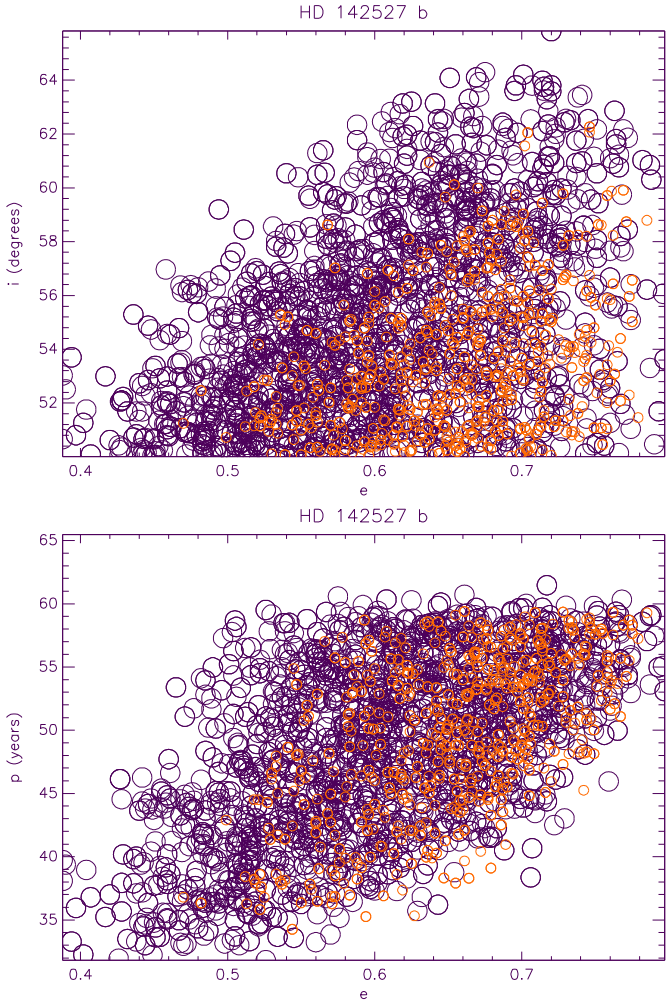

Figure 4.17: Orbital parameter correlation for HD142527b

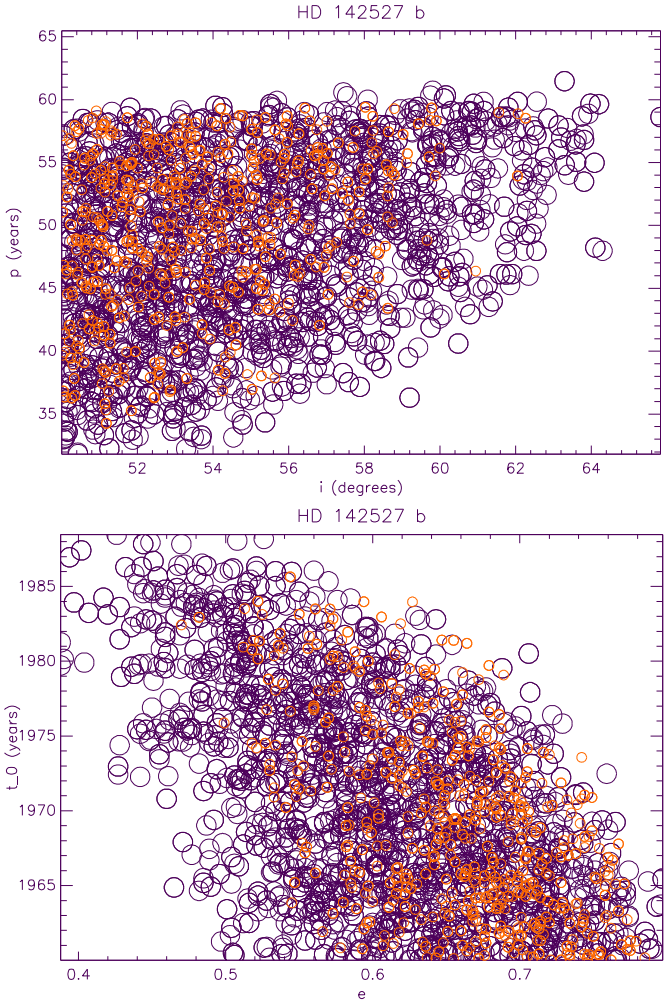

Figure 4.18: Orbital parameter correlation for HD142527b

This parameter is used both for the circumbinary objects and the circumstellar object. In this case, it will be analyzed only the circumbinary one. There are also two other important limitation:

- Although binaries typically have eccentric orbits, most of the analytic results of the literature have been developed for the case of binaries with circular orbits.
- Numerical investigations of stability have been restricted to special cases such as binary systems with equal mass stars or particular binary systems [41], like HD142527

The two limitations above were provided to not be of greatest impact on this work final result, as it was taken into account to work with eccentricity intervals in accord to my results.

So Holman et al (2008) started a simulation with test particles and saw which particles survives in the orbit for a typical integration time and which not: so the semimajor axis at which the test particles at all initial longitudes survived the full integration time is called the critical semi-major axis. Above this number, the particle wouldn't stay in the orbit. In other words a_c can be simply refered as a stability limit for a given orbit with given orbital parameters.

So how it is determined? In their experiments, Holman et al (2008) found that there was a correlation of the a_c and both the e (eccentricity) and μ (reduced mass of the binary system). In this way, their final result, after analyizing it for 10^4 full time integrated binary star, was (for a circumbinary orbit):

$$a_c = (1.60 + 5.10\ e - 2.22\ e^2 + 4.12\ \mu - 4.27\ \mu e - 5.09\ \mu^2 + 4.61\ e^2\mu^2)a \qquad (4.1)$$

where a is the orbit semi-major axis.

A further element of discussion is on the dynamical limit of the binary system. In fact as $(1-\mu)$ and $\mu \to 0$, one would expect the critical semimajor axis to scale as with the Hill's sphere as $(1-\mu)^{\frac{1}{3}}$. However this condition is not verified as can be seen in [fig:4.19].

Analyzing the Hill Sphere limits, according to the expression of a_c and Holman results, there are two distinct dynamical regimes for a possible third-particle stability, one where $(1-\mu)$ and $\mu \ll 1$ and one for $\mu \sim 0.5$, with the switch occuring near where $(1-\mu)$ and $\mu \sim 0.2$.

So, for HD 142527, the results of the Monte Carlo simulation gives that the semi-major axis is lesser than the critical semi-major axis as expected for the circumbinary case. In our case, we are aiming to determine the stability limit around the central binary. As the binary orbit is not firmly known, we derived a_c for each set of orbital parameter in the MC simulation, as in [fig:4.20].

The mean values are $a = 0.126 \pm 0.012\ arcsec$ and $a_c = 0.353 \pm 0.053\ arcsec$ (or $51.19\ au$), the max value of the critical semi-major axis is: $a_{c,max} = 0.48\ arcsec$. This point is confirmed more by the Monte Carlo simulation, where the high e and, relatively for this study, little period give a severe limit to the orbital amplitude.

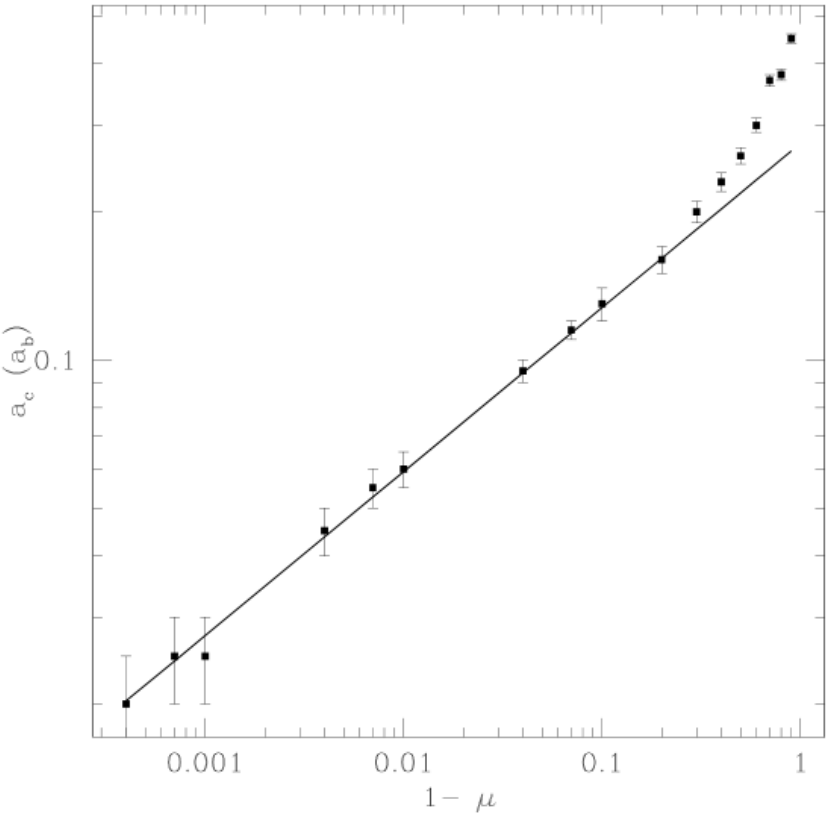

Figure 4.19: The critical semimajor axis a_c as a function of $(1-\mu)$ for the binary eccentricity $e = 0$. The heavy line indicates the $(1-\mu)^{\frac{1}{3}}$ dependence of the Hill's sphere. The error bars used in this figure indicates the full separation between simulated particles of Holman (2007): if the particle separation is 0.01 a_b , the error bars span ± 0.01 a_b

As the inner edge of the outer disk is at 0.89 *arcsec* ($\sim$ 130 *au*) [32], this also means that it's highly probable that the star's companion cannot be responsable for the gap between the inner and outer disk.

The possibility that the binary companion in its current orbit is responsible for the location of the inner edge of the disk is excluded. Following, there are a few possible reason that explains how the gap came up, but that are neglected because of the reason explained subsequently:

- The photoevaporation can explain holes up to $\sim$ 20 *au* in accreting and even larger holes for non- accreting disks [42] [43] but it can not explain the gap in HD142527, which has an accretion rate of 6.9 $10^{-8} M_{\odot}\ yr^{-1}$ [44] and a very large hole. Photoevaporation would also not explain why there should still be an inner disk, which would be expected to clear on a a viscous timescale of $t_{visc} \sim 10^5\ yr$.

- Dust grain growth is an unlikely explanation for the gap because it is also seen

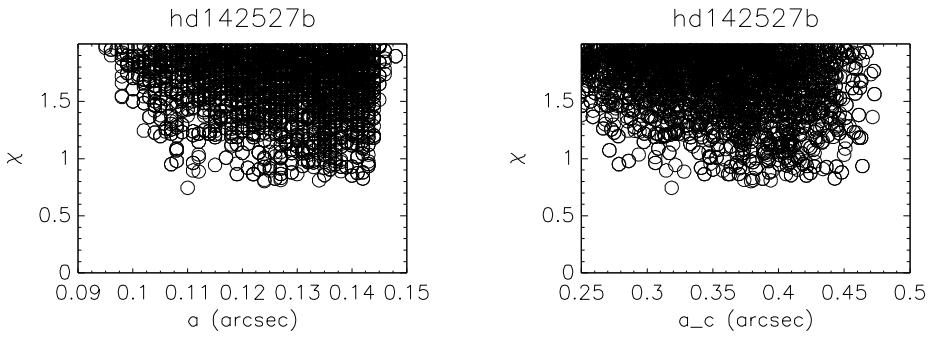

Figure 4.20: The semi-major axis and the critical semi-major axis vs the χ^2_{red}. The values are 3 times different, and so it's impossible to obtain a critical orbit for HD142527b

in the sub-mm [45] ,meaning that the surface density of mm-sized grains is low. [47]

- The dynamical clearing by a companion object: the warp inside the cavity of HD 142527, i.e. the continuous change in inclination at some specific radius, should significantly impact the observed kinematics. So the Keplerian movement should be highly perturbated. Given this orientation, we can rule out an outflowing disk wind: the velocity component orthogonal to the disk would broaden the lines and preserve reflection symmetry about the outer disk PA, while the radial component in the plane of the disk would twist the kinematics in the opposite direction than observed. [49]

Moreover, one way of discriminating between a planet-induced gap and a photoevaporation-induced one can be based on the sharpness of the transition in surface density at the outer edge of the cavity: dynamical clearing would result in a rather sharp transition if the putative planet is massive. So the best planet, if present, should be likely a Jupiter type.

The planet should be the one of the greatest possibilities then. However, as explained before, there is no decisive evidence of it on the observational point of view, but there are indirect, but no decisive, evidences of a possible planet:

- The presence of a giant planet follows a general drop in density inside the 90 au cavity. The polarimetric data provides upper limits on the surface brightness of the polarized intensity emitted from inside the cavity confirm this [48]

- Non-axial symmetry in the cavity can be a signature of obscured planet [46].
- Another non-direct planet existence hint is the imprinted "marks" on their progenitor disk. Wide gaps will be carved by massive or multiple forming planets [49]
- The shape of the outer disk inner wall will depend on the planet mass, disk thickness and viscosity of the disk, and on the temperature structure in the disk wall itself [50]. The torque of the outermost planet will affect strongly the shape of the inner wall.

The hypotesis of the presence of a circumbinary planet in the outer region is explored in the conclusion.

Chapter 5

Conclusion

The result data from HR8799 are in agreement with the previous data of Zurlo et al (2015). This was indeed predicted, because the code was already used for this system in the Esposito et al (2013). The study of the orbital parameters has reduced the range interval, but the presence of the planet f can change the result. Future observations will help to solve this point.

The data from Beta Pictoris are in agreement with the previous data of Wang et al (2016). Even in this case the result was predicted. Also the strong limitations on the possible orbits gave an hard time for the code, and this had been shown by the lesser density of data in its Monte Carlo simulation compared to the ones of the other two stellar system.

The data from the HD 142527 study, which have all non-coronagraph observation, give an important test for the disk structure: a first PCA [fig:5.1] (principal component analysis) was done in 2014 (Gratton R. priv. com.), in order to detect an additional companion beside the known M dwarf. The PCA is a statistical procedure that uses an orthogonal transformation to convert a set of observations of possibly correlated variables into a set of values of linearly uncorrelated variables called principal components. In short, it's used to find a pattern between parameters. In the region outside the coronagraphic mask (~ 0.12 *arcsec* from the star) there was no detection. The upper limits where in bandwith $\Delta J = 13.5$ *mag* at a separation of 0.5 *arcsec* (72.5 *au*). This means no companion more massive than $M_J = 14.3\ M_\oplus$.

More recent data on this problem have been obtained, and the result are in [fig:5.2]:

This data compare the limit mass of the observation and the separation. It's possible to see that the first result is the probable location of the planet. The stability limit starts at 0.25 *arcsec* (the minimum value of a_c), has a mean value of $a_c = 0.35$ and finishes at 0.48 *arcsec* (the max value of a_c), while the start of the outer disk is at 0.9 *arcsec*. The last three values are enlighted by the green, black and red lines in [fig:5.2]. In this situation, a planet with mass $\leq 10\ M_J$ at an angular separation of $0.25 - 0.9$ *arcsec* can be responsible for the gap and can have escaped detection in SPHERE images. The second result is the mass limit for the planet.

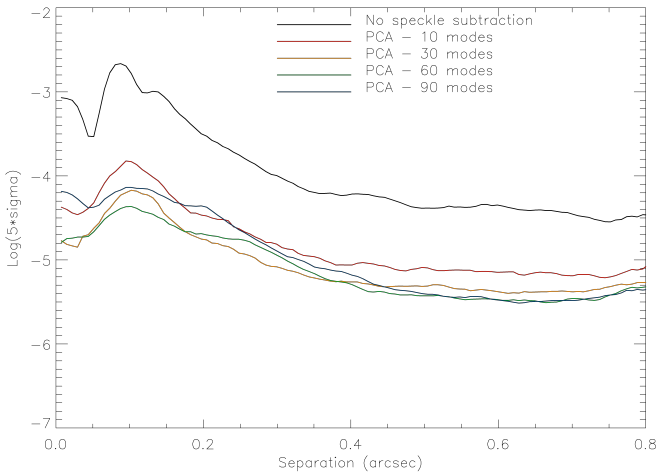

Figure 5.1: 5-sigma limiting contrast curve obtained from the IFS Y-J observation of HD142527 using the PCA procedure. All curves are corrected for self-cancellation using artificial stars. No companion was detected down to this limit in the region outside the coronagraphic mask (separation of 0.12 arcsec from the star). Credits to Gratton Raffaele.

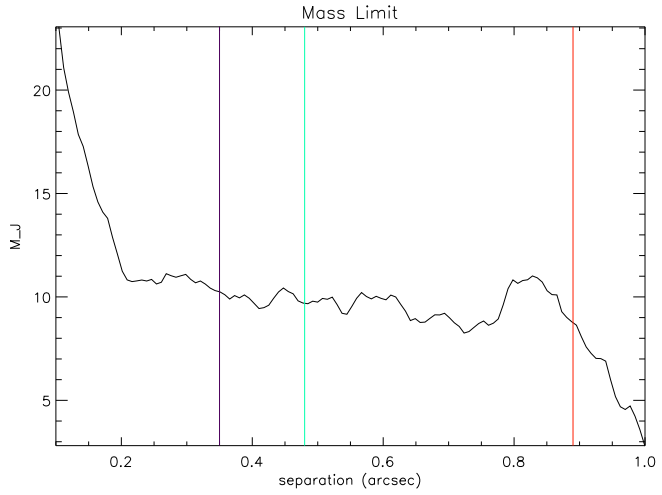

Figure 5.2: The separation and mass limit for the IFS-SPHERE observation (2016). The first and the last part, in which the line tends to infinity, are the IFS observational limits.

In the end, the code gave an important result for a further characterization of HD142527, and set off the possibility in which the star companion would be the responsible for the gap but likely a new planet. Moreover, the study of the critical semi-major axis of the binary gives an important hint on the possibility of the planet location.

Bibliography

[1] Appunti di astrofisica relativistica (Relativistic Astrophysics notes). Private notes, contact doctor Taverna Roberto, Physics department, Padua University

[2] Lecture of Star Formation. Private lectures, contact doctor Chiosi Cesare, Padua University

[3] Protoplanetary Disks and their Evolution, Williams and Ceiza, notes from the Institute for Astronomy, University of Hawaii, Honolulu, HI 96822, USA

[4] Zsom et al, 2010 A& A,26A,513A,56G

[5] Nelson et Papaloizu et al, 2005: http://stacks.iop.org/RoPP/69/119

[6] Masset et al, 2006, ApJ, 607, 155

[7] Lubow et al, 2010, ApJ, 1004, 4137

[8] Chauvin et al 2004, ApJ, 0409, 9323

[9] Ragazzoni Astrophysic Laboratory I, private notes, contact the professor

[10] Marzari Lectures, Physics department, Padua University

[11] Marois et al, 2005, ApJ, 556, 564

[12] Racine et al, 1999, 587, 594

[13] Thatte et al., 2007, MNRAS, 379, 1229

[14] Methods of detecting exoplanets, Bozza, Mancini, Sozetti, ed. Springer, 2016

[15] The exoplanet Handbook, Perryman, ed. Cambridge, 2011

[16] Quanz et al. 2011, ApJ 738, 23

[17] Guyon et al., 2006

[18] Soummer et al, 2013

[19] http://www.amnh.org/our-research/physical-sciences/astrophysics/research/project-1640

[20] planetimager.org

[21] Beuzitet et al, 2008

[22] Thalmann et al,2008, SPIE, 7015

[23] Dohlen et al, 2014, SPIE, 2014

[24] Claudi et al, 2010, SPIE, 7014

[25] Macintosh et al, 2014

[26] Maire et al. 2015, A&A, 576, A133

[27] Gray et al, 1999, ApJ, 118, 2993

[28] Marois et al, 2010, Nature, 1011, 4918

[29] Barman et al, 2011, ApJ, 1103, 3895

[30] Su et al, 2009, ApJ, 909, 2687

[31] Esposito et al, 2013, A&A, 549, A52

[32] Zurlo et al, 2015, A&A, 1511, 4083

[33] Hanh, 2010, ApJ, 1006, 4311

[34] Wang et al, 2016, 1607, 5272

[35] Lacour et al, 2016, 1511, 9390

[36] Double Stars, Heintz, Reidel, 1976

[37] $http://www.gemini.edu/images/pio/News/2014/pr2014\_01/BetaPic.jpg$

[38] Grey et al, 2006, ApJ, 603, 770

[39] Cassus et al, 2012, ApJ, 1207. 2056

[40] Soummer et al., 2011

[41] Holman and Wiegert, ApJ, 2008, 980, 9315

[42] Owen et al, 2011

[43] Dominik & Dullemond, 2011

[44] Garcia Lopez et al, 2006

[45] Casassus et al, 2013

[46] Casassus et al, 2015, ApJ,1505, 7732

[47] Chiang & Murray-Clay, 2007

[48] Avenhaus et al, 2013, ApJ, 1311, 7088

[49] Dodson-Robinson, S. E., & Salyk, 2011, ApJ, 738, 131

[50] Crida et al. 2006